

Semianalytical estimates of scattering thresholds and gravitational radiation in ultrarelativistic black hole encounters

Emanuele Berti^{1,2*}, Vitor Cardoso^{1,3}, Tanja Hinderer², Madalena Lemos³, Frans Pretorius⁴, Ulrich Sperhake^{1,2,5}, Nicolás Yunes⁴

¹ *Department of Physics and Astronomy, The University of Mississippi, University, MS 38677, USA*

² *California Institute of Technology, Pasadena, CA 91109, USA*

³ *CENTRA, Dept. de Física, Instituto Superior Técnico, Av. Rovisco Pais 1, 1049 Lisboa, Portugal*

⁴ *Department of Physics, Princeton University, Princeton, NJ 08544, USA and*

⁵ *Institut de Ciències de l'Espai (CSIC-IEEC), Facultat de Ciències, Campus UAB, Torre C5 parells, Bellaterra, 08193, Spain*

Ultrarelativistic collisions of black holes are ideal gedanken experiments to study the nonlinearities of general relativity. In this paper we use semianalytical tools to better understand the nature of these collisions and the emitted gravitational radiation. We explain many features of the energy spectra extracted from numerical relativity simulations using two complementary semianalytical calculations. In the first calculation we estimate the radiation by a “zero-frequency limit” analysis of the collision of two point particles with finite impact parameter. In the second calculation we replace one of the black holes by a point particle plunging with arbitrary energy and impact parameter into a Schwarzschild black hole, and we explore the multipolar structure of the radiation paying particular attention to the near-critical regime. We also use a geodesic analogy to provide qualitative estimates of the dependence of the scattering threshold on the black hole spin and on the dimensionality of the spacetime.

PACS numbers: 04.25.D-, 04.25.dc, 04.25.g, 04.25.dg, 04.50.Gh, 04.60.Cf, 04.70.-s

I. INTRODUCTION

Solving Einstein’s equations numerically is a highly nontrivial task. After the recent breakthroughs in numerical relativity (NR) [1–3], binary black hole (BH) mergers have been routinely carried out by several groups worldwide. As is often the case in physics, the results of numerical simulations are best understood or interpreted by studying simplified models that capture the main features of the problem. In this paper we will argue that semianalytical tools are particularly useful to gain insight into the fascinating but complex problem of ultrarelativistic BH collisions.

High-energy BH encounters are a difficult undertaking in NR (see Refs. [4–7] for a discussion of ultrarelativistic collisions in four dimensions, Refs. [8–11] for recent progress on D -dimensional simulations and Ref. [12] for a review of the most outstanding questions in ultrarelativistic BH collisions before the recent breakthroughs in NR). Efficient adaptive mesh refinement and wave extraction techniques are required because the problem involves various scales: the BHs are “pancake-shaped” because of Lorentz contraction, the large speeds involved in the collision require large initial separations to define asymptotic states, and high resolution is required to study the dynamics of the final BH (if any) formed as a result of the merger. Further difficulties arise from the spurious radiation present in the initial data.

Despite their relatively limited accuracy, simulations

of ultrarelativistic BH collisions to date have provided definite predictions for nonspinning BHs in four dimensions [4–7]. For example these simulations show that, even in the highly symmetric case of head-on collisions, as much as $\sim 14 \pm 3\%$ of the energy of the system can be radiated in gravitational waves [4, 5]. They further demonstrate the existence of three distinct regimes depending on the impact parameter b : immediate mergers, nonprompt mergers and the scattering regime. These regimes are separated by two special values of the impact parameter: the *threshold of immediate merger* b^* and the *scattering threshold* b_{scat} . Roughly speaking, for $b < b^*$ merger occurs within the first encounter, whereas for $b^* < b < b_{\text{scat}}$ it does not, but sufficient energy is radiated to put the binary into a bound state that eventually results in a merger. For the largest initial center of mass velocities of $v = 0.94$ studied to date, as much as $\sim 35 \pm 5\%$ of the energy can be carried away by gravitational radiation [5, 6].

Close to the threshold of immediate merger, the binary exhibits “zoom-whirl” behavior, an extreme version of relativistic perihelion precession which can be precisely defined and understood in the geodesic limit [13–17]. For point particles orbiting BHs, zoom-whirl orbits are intimately related to the existence of unstable spherical orbits (unstable *circular* orbits at radii $3M \leq r \leq 6M$ in the special case of Schwarzschild BHs). The very existence of zoom-whirl orbits in comparable-mass BH encounters is perhaps a strong hint that simple, semianalytical approaches (in this case, the study of point-particle geodesics around BHs) can provide valuable insight into the general solution of the problem.

NR simulations of ultrarelativistic BH collisions have

*Electronic address: berti@phy.olemiss.edu

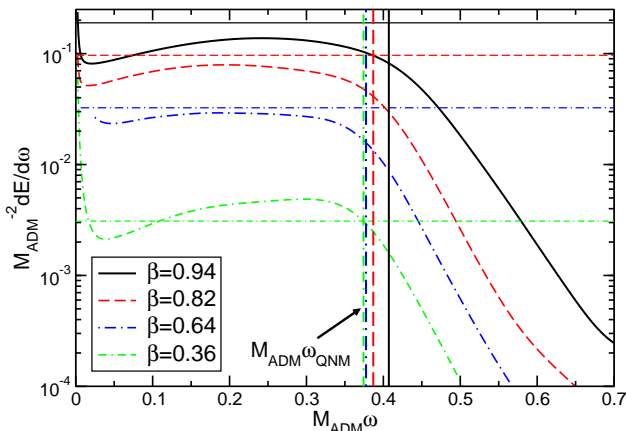


FIG. 1: Energy spectrum for the dominant (quadrupolar, i.e. $l = 2$) component of the gravitational radiation computed from NR simulations of the head-on collision of two equal-mass BHs (from [4]). The collision speed in the center-of-mass frame, $\beta = v/c$, is indicated in the legend. The energy spectrum is roughly flat (independent of frequency) up to the quasinormal mode (QNM) frequencies (marked by vertical lines), after which it decays exponentially. All quantities are normalized to the Arnowitt-Deser-Misner (ADM) mass of the system M_{ADM} .

also provided information on the structure of the Fourier-domain energy spectra $dE^{\text{rad}}/d\omega$. An interesting feature of the spectra of comparable-mass BH collisions is the presence of a nonvanishing zero-frequency limit (ZFL). For head-on collisions, Fig. 1 shows that the energy spectrum is roughly flat (independent of frequency) up to some cutoff frequency, after which it decays exponentially (in this figure and elsewhere in the paper we use geometrical units $G = c = 1$). Grazing ultrarelativistic BH collisions also lead to energy spectra with complex features, although this was not discussed in Ref. [6] because of space limitations. These complex spectra are discussed further in section V of the present work.

One of the motivations of this paper is to explore simplified, analytical and semianalytical descriptions of ultrarelativistic BH mergers that provide qualitative (and sometimes even quantitative) explanations of the main features of these spectra [4]. In particular, we shall concentrate on the combination of the following two approaches: a linearized calculation in flat spacetime pioneered by Weinberg and Smarr [18–21] and BH perturbation theory [22–28]. We will refer to the Weinberg-Smarr approach (which is valid for arbitrary velocities, as long as the radiated energies are small) as the “ZFL calculation,” because it provides a good approximation of the emitted energy spectrum at low frequencies. The ZFL calculation assumes an instantaneous collision in flat

spacetime, and in four dimensions it yields a flat spectrum *at all frequencies* – precisely what one would expect from the analogous problem in electromagnetism [29]. The origin of the exponential cutoff in the NR spectra can be understood through the second approach, i.e. by computing the radiation from point particles falling in a *curved* BH spacetime [22–28]. These perturbative calculations show that the radiation in a given multipole “shuts off” at the real part of the lowest QNM frequency of the BH for the multipole in question [30, 31].

In this paper we address several questions related to the puzzling behavior of ultrarelativistic BH collisions:

1. We use geodesic calculations to explore the dependence of the scattering threshold on BH spin and dimensionality of the spacetime. This threshold determines whether the two BHs will eventually merge or not, and it is of fundamental importance to estimate cross sections for BH production in high-energy collisions [32]. Classical general relativity in D dimensions should be adequate to determine the cross section for BH production at trans-Planckian collision energies and the fractions of the collision energy and angular momentum lost in gravitational radiation. This information will be of paramount importance to improve the modeling of microscopic BH production in event generators such as TRUENOIR, CHARYBDIS2, CATFISH or BLACKMAX [33–36]. The event generators will then provide a description of the corresponding evaporation phase, which might be observed during LHC collisions.
2. We reproduce the qualitative (and sometimes quantitative) features of the energy spectra by a “bare-bones” approach, where we replace the colliding BHs by two point particles and we estimate the radiation by a ZFL calculation with *finite* impact parameter. The generalization to finite impact parameter requires a specific model to bind the particles after the collision and guarantee energy-momentum conservation [37], but our qualitative conclusions should be roughly independent of the details of the model.
3. We gain insight into the details of the emitted radiation (particularly in the near-critical regime) by a perturbative study of the ultrarelativistic infall of point particles with generic impact parameter into a Schwarzschild BH.

The two-pronged analytical approach above provides a better understanding of most of the main features of the energy spectra. In particular, we reach the following conclusions:

- i. In both the extreme-mass ratio case and in comparable-mass NR simulations, the ZFL is by and large independent of the impact parameter b .

- ii. For a given multipolar index l , the slope of the different m -components at low frequencies is proportional to b .
- iii. The exponential cutoff is related to the QNM frequencies of the final BH.
- iv. Higher multipoles of the radiation become increasingly important as the binary becomes ultrarelativistic, leading from an exponential scaling of the form $e^{-a_R l}$ in the nonrelativistic limit to a scaling of the form b_R/l in the ultrarelativistic limit, where (a_R, b_R) are constants.
- v. The total radiation is proportional to the number of orbits near the scattering threshold for *nonrelativistic* infalls, but it is enormously enhanced (essentially by a resonance with the QNM frequencies of the final BH) when the collision is ultrarelativistic.

The plan of the paper is as follows. In section II we compute the critical impact parameter for geodesics in four and higher dimensions. In section III we explore a simple toy model to estimate the radiation in the ZFL for collisions with finite impact parameter. In section IV we compute the energy, angular momentum and linear momentum radiated by point particles falling into Schwarzschild BHs in four dimensions with arbitrary energy. In section V we show how the ZFL and point-particle calculations shed light on some features of NR simulations of ultrarelativistic BH collisions. We conclude by pointing out possible extensions of our investigation. Appendix A gives some technical details on the Sasaki-Nakamura formalism, and Appendix B shows how the ZFL results can be decomposed in terms of spin-weighted spherical harmonics.

We work mostly in four spacetime dimensions with signature $(-, +, +, +)$ [38], except for the discussion in section II C, where we explore higher-dimensional BHs. Greek letters (μ, ν, \dots) in index lists range over all spacetime indices. The Einstein summation convention is employed unless otherwise specified. Overhead dots stand for partial differentiation with respect to the proper time τ , $\dot{E} \equiv \partial E / \partial \tau$; $\mathcal{O}(A)$ stands for terms of order A .

II. SCATTERING THRESHOLD IN BLACK HOLE SPACETIMES

One of the main ingredients to estimate BH production rates in particle accelerators is the cross section for BH production [32]. Several analytical approximations have been used to estimate cross sections [12]. In this section we explore a particularly simple approach. We compute the critical impact parameter between plunge and scattering for particles following geodesics in different BH metrics, in order to estimate the qualitative dependence of the cross section on BH spin and dimensionality. We begin with a brief review of the scattering

threshold in the Schwarzschild background. Then we proceed to the computation of the critical impact parameter in a four-dimensional rotating (Kerr) background, and finally we generalize the analysis to higher-dimensional rotating (Myers-Perry) backgrounds.

A. Schwarzschild black holes

Geodesics in a Schwarzschild background are completely determined by their energy and (z -component of) orbital angular momentum per unit rest mass. It is useful to replace the total energy \tilde{E} and the orbital angular momentum \tilde{L}_z by the parameters $E = \tilde{E}/\mu$ and $L_z = \tilde{L}_z/\mu$. Here μ is the particle's rest mass and E is related to the velocity v of the particle at infinity by $E = (1 - v^2)^{-1/2}$. The geodesic radial behavior is governed by the relation $(dr/d\tau)^2 = E^2 - V_{\text{eff}}(r, L_z)$, where τ is the proper time and the effective potential for a Schwarzschild background is $V_{\text{eff}} = (1 + L_z^2/r^2)f$, with $f \equiv 1 - 2M/r$ and M the BH mass.

Geodesics can be classified according to how their energy compares to the maximum value of the effective potential, which in this case is given by

$$V_{\text{eff}}^{\text{max}} = \frac{1}{54} \left[\frac{L_z^2}{M^2} + 36 + \left(\frac{L_z^2}{M^2} - 12 \right) \sqrt{1 - \frac{12}{(L_z^2/M^2)}} \right]. \quad (1)$$

The scattering threshold is then defined by the condition $E^2 = V_{\text{eff}}^{\text{max}}$: unbound orbits with $E^2 > V_{\text{eff}}^{\text{max}}$ are captured, while those with $E^2 < V_{\text{eff}}^{\text{max}}$ are scattered. Given some E , the critical radius or impact parameter b_{crit} that defines the scattering threshold is obtained by solving the condition $E^2 = V_{\text{eff}}^{\text{max}}$ for $L_z = L_{\text{crit}}$, and then using the relation

$$b_{\text{crit}} = L_{\text{crit}}(E^2 - 1)^{-1/2}. \quad (2)$$

Note that we mostly work in the point particle approximation with no radiation reaction effects, so we adopt a slightly different terminology from that of Ref. [6]: here L_{crit} denotes the critical angular momentum separating plunging trajectories from scattering trajectories.

Ultrarelativistic collisions can be modeled by large-energy geodesics. One can then show that a high-energy orbit plunges when

$$\frac{L_z^2}{M^2} < \frac{L_{\text{crit}}^2}{M^2} \simeq \frac{27}{(1/E^2)} - 9 - \frac{1}{E^2} + \mathcal{O}(1/E^4), \quad (3)$$

where the last relation is valid in the limit $E^2 \gg 1$. The condition for scattering is $L_z > L_{\text{crit}}$. One can also easily show that all orbits plunge if $L_z^2 < 12M^2$ when the particle is at rest at infinity ($E = 1$). If $E > 1$, scattering orbits exist only if $L_z > 4M$.

B. Kerr black holes

The radial motion of equatorial geodesics in a Kerr background can also be described in terms of an effective potential [39]. In this case, however, the potential for timelike geodesics takes a more complicated form, which we can parametrize as

$$V_{\text{eff}} = \left(1 + \frac{L_z^2}{r^2}\right) f + j \frac{\sigma_1 L_z}{r^3} + j^2 \left(\frac{\sigma_2}{r^2} + \frac{\sigma_3}{r^3}\right). \quad (4)$$

The Kerr spin parameter a and the reduced spin parameter j are related to the spin angular momentum J via $J = Ma = jM^2$. As before, E and L_z stand for the energy and (z -component of) angular momentum per unit rest mass. For convenience, we have also defined the energy-dependent ‘‘spin-deformation’’ parameters

$$\sigma_1 \equiv 4M^2 E, \quad \sigma_2 \equiv M^2 (1 - E^2), \quad \sigma_3 \equiv -2M^3 E^2. \quad (5)$$

For fixed j , orbits with a turning point are identified by pairs (E, L_z) for which V_{eff} has a double root. The extrema of the effective potential are defined by

$$\frac{dV_{\text{eff}}}{dr} = \frac{2M}{r^2} + \frac{6ML_z^2}{r^4} - \frac{2L_z^2}{r^3} - \frac{3j\sigma_1 L_z}{r^4} - j^2 \left(\frac{2\sigma_2}{r^3} + \frac{3\sigma_3}{r^4}\right) = 0 \quad (6)$$

and correspond to radii

$$r_{\pm} = \frac{L_z^2}{2M} \left(1 + j^2 \frac{\sigma_2}{L_z^2}\right) \pm \frac{L_z^2}{2M} \left[1 - \frac{12M^2}{L_z^2} + j \frac{6M\sigma_1}{L_z^3} + j^2 \left(\frac{2\sigma_2}{L_z^2} + \frac{6M\sigma_3}{L_z^4}\right) + j^4 \frac{\sigma_2^2}{L_z^4}\right]^{1/2}. \quad (7)$$

The maximum of the effective potential is then equal to $V_{\text{eff}}^{\text{max}} = V_{\text{eff}}(r = r_-)$, which generalizes Eq. (1).

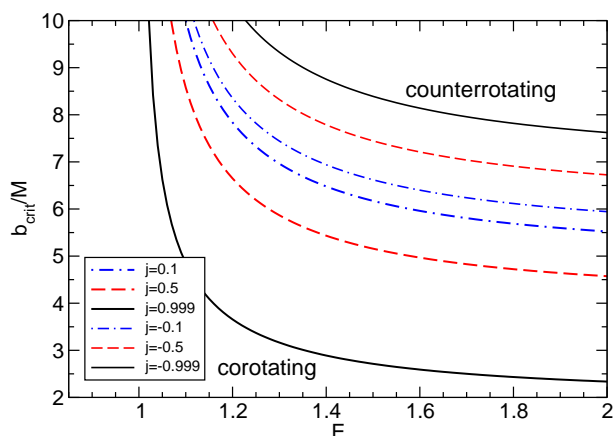


FIG. 2: Critical impact parameter versus reduced energy E for different values of j in a Kerr background.

If we are given some values of (E, j) , the critical impact parameter b_{crit} can be obtained by solving $E^2 = V_{\text{eff}}^{\text{max}}$ for

L_{crit} , and then using Eq. (2). Figure 2 plots this critical impact parameter as a function of energy for different values of the spin, where we have solved for b_{crit} numerically. Observe that b_{crit} asymptotes rapidly to a constant as the energy approaches $E \sim 2$. For large, positive spins (co-rotating case), the critical impact parameter asymptotes to $b_{\text{crit}} \sim 2.33M$ for $E = 2$, while for large, negative spins (counter-rotating case) it asymptotes to $b_{\text{crit}} \sim 7.62M$. As the spin is decreased, the critical impact parameter for corotating geodesics increases, so that the smallest impact parameter corresponds to maximally spinning BHs.

The above considerations suggest that an asymptotic analysis might allow for a better analytical understanding of the critical impact parameter in the ultrarelativistic regime. Let us then define the perturbation parameters

$$1 \gg \epsilon \equiv 1 - j > 0, \quad 1 \gg \xi \equiv 1/E > 0. \quad (8)$$

Performing an asymptotic expansion to second order in ϵ , the solution to $E^2 = V_{\text{eff}}^{\text{max}}$ becomes

$$L_{\text{crit}} \sim \frac{2}{\xi} + \sqrt{\epsilon} \frac{\sqrt{6 - 2\xi^2}}{\xi} + \epsilon \frac{2(\xi^2 - 1)}{\xi(\xi^3 - 3)} + \epsilon^{3/2} \frac{(\xi^2 - 1)(3\xi^4 + 5)\sqrt{6 - 2\xi^2}}{\xi(\xi^2 - 3)^3} + \mathcal{O}(\epsilon^2). \quad (9)$$

Reexpanding this equation to second order in ξ , we find

$$\frac{b_{\text{crit}}}{M} \sim 2 + \sqrt{6}\sqrt{\epsilon} + \frac{2}{3}\epsilon + \frac{5\sqrt{6}}{108}\epsilon^{3/2} + \left(1 + \frac{\sqrt{6}}{3}\sqrt{\epsilon} - \frac{1}{9}\epsilon + \frac{5\sqrt{6}}{324}\epsilon^{3/2}\right)\xi^2 + \mathcal{O}(\epsilon^2, \xi^3). \quad (10)$$

Eq. (10) is formally a bivariate expansion, i.e. an expansion in two independent perturbation parameters: ϵ and ξ . This expansion is a fractional Frobenius series, with the regular limit $b_{\text{crit}} \rightarrow 2$ when $\epsilon \rightarrow 0$ and $\xi \rightarrow 0$. The energy parameter contributes only to second order, while the spin contributes at fractional leading order. A comparison of this estimate to the numerical solution of Fig. 2 shows good agreement: when $j = 0.999$ and $E = 2$ Eq. (10) predicts $b_{\text{crit}} \sim 2.335M$, while the numerical result is $b_{\text{num}} = 2.396M$. Therefore the relative fractional error of the asymptotic expansion (dominated by the neglected relative E^{-3} terms) is approximately 2.6%.

In the ultrarelativistic limit ($\xi \rightarrow 0$), we can solve the critical impact parameter equation exactly for arbitrary j to find [39]

$$\frac{b_{\text{crit}}}{M} = -j + 6 \cos \left[\frac{\arccos(-j)}{3} \right], \quad (11)$$

or alternatively $b_{\text{crit}}/M = -j + 3x + 3/x$, where $x \equiv [-j + (j^2 - 1)^{1/2}]^{1/3}$. The asymptotic expansion is very accurate in the ultrarelativistic limit: for example, for $j = 0.999$ this exact formula gives $b_{\text{crit}}/M = 2.07812987$, to be compared with $b_{\text{crit}}/M \sim 2.07812992$ from Eq. (10).

C. Myers-Perry black holes

We now generalize the above analysis to higher-dimensional BHs, considering for illustration the Myers-Perry solution with a single angular momentum direction [40]. The metric of a D -dimensional Kerr BH with only one nonzero angular momentum parameter is given in Boyer-Lindquist-type coordinates by [40]

$$ds^2 = -\frac{\Delta - a^2 \sin^2 \vartheta}{\Sigma} dt^2 - \frac{2a(r^2 + a^2 - \Delta) \sin^2 \vartheta}{\Sigma} dt d\varphi + \frac{(r^2 + a^2)^2 - \Delta a^2 \sin^2 \vartheta}{\Sigma} \sin^2 \vartheta d\varphi^2 + \frac{\Sigma}{\Delta} dr^2 + \Sigma d\vartheta^2 + r^2 \cos^2 \vartheta d\Omega_{D-4}^2, \quad (12)$$

where

$$\Sigma = r^2 + a^2 \cos^2 \vartheta, \quad (13)$$

$$\Delta = r^2 + a^2 - M_* r^{5-D}, \quad (14)$$

$d\Omega_{D-4}^2$ denotes the standard metric of the unit $(D-4)$ -sphere, and M_* is related to the BH mass. In fact this metric describes a rotating BH in an asymptotically flat vacuum spacetime with mass \mathcal{M} and angular momentum \mathcal{J} given by

$$\mathcal{M} = \frac{D-2}{16\pi} A_{(D-2)} M_*, \quad \mathcal{J} = \frac{1}{8\pi} A_{(D-2)} M_* a, \quad (15)$$

where $A_{(D-2)}$ is the area of a unit $(D-2)$ -sphere:

$$A_{(D-2)} = \frac{2\pi^{(D-1)/2}}{\Gamma[(D-1)/2]}. \quad (16)$$

Timelike equatorial geodesics depend on the effective potential

$$V_{\text{eff}} = r^2 E^2 + \frac{M_*}{r^{D-3}} (aE - L_z)^2 + (a^2 E^2 - L_z^2) - \delta_1 \Delta_D, \quad (17)$$

where D is the dimensionality of spacetime and $\Delta_D = r^2 + a^2 - M_* r^{5-D}$. For $D=4$, the quantity M_* and the mass of the BH are related via $M_* = 2\mathcal{M}$. In higher dimensions M_* does not have units of length, but instead $[M_*] = (\text{length})^{D-3}$. We also introduce a dimensionless spin parameter

$$j = \frac{a}{(M_*/2)^{1/(D-3)}}, \quad (18)$$

which reduces to the corresponding Kerr quantity for $D=4$.

When $D=5$ we can carry out an asymptotic analysis similar to the one presented in the previous subsection (see also [41]). In the ultrarelativistic limit ($E \rightarrow \infty$) we have

$$b_{\text{crit}}^{(D=5)} / \sqrt{M_*} = 2 - j/\sqrt{2}, \quad (19)$$

which is to be contrasted with the four-dimensional result presented in Eq. (11). This asymptotic analysis reveals that both in four and five dimensions the overall effect of spin for corotating geodesics is to reduce the critical impact parameter, suggesting that the highest energy emission occurs for maximally rotating BHs.

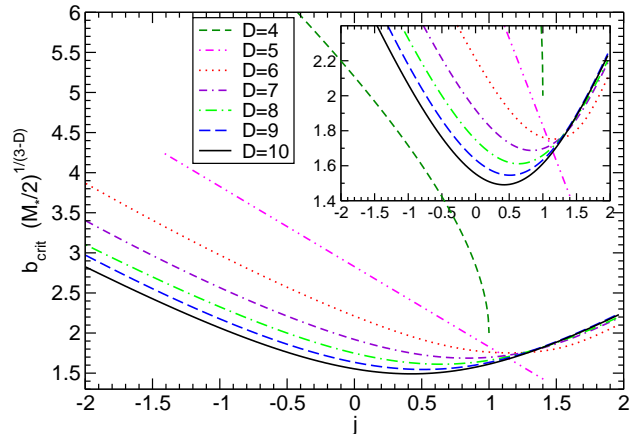


FIG. 3: Critical impact parameter for $E=10$ as a function of j for Myers-Perry BHs in different dimensions D . The inset zooms along the y -axis to show the local minima more clearly.

For dimensions higher than five, an asymptotic analysis is more involved due to the higher inverse polynomial order of the effective potential. However, a numerical calculation is straightforward. In Fig. 3 we plot the dimensionless impact parameter $b_{\text{crit}}/(M_*/2)^{1/(D-3)}$ as a function of j for different values of D . The calculations in Fig. 3 refer to $E=10$, but this is already a good approximation of the asymptotic value of the impact parameter in the ultrarelativistic region. Observe that as D increases, the minimum in $b_{\text{crit}}/(M_*/2)^{1/(D-3)}$ corresponds to smaller values of j .

The (v, j) phase space is explored in more detail in Fig. 4, where we show contour plots of the dimensionless impact parameter for both corotating and counterrotating geodesics in different dimensions. Note that the smallest critical impact parameter corresponds to corotating, ultrarelativistic geodesics, but the BH must not necessarily be maximally spinning when $D > 5$. For $6 \leq D \leq 10$ the critical impact parameter presents a local minimum $b_{\text{crit}}^{\text{min}}$ as a function of j , which is well described by the following quadratic fit:

$$b_{\text{crit}}^{\text{min}} \left(\frac{M_*}{2} \right)^{\frac{1}{3-D}} = 3.978 - 0.679D + 0.033D^2. \quad (20)$$

This fit was constructed considering only spacetimes with $D \leq 10$, so its extrapolation to $D > 10$ should be used with caution.

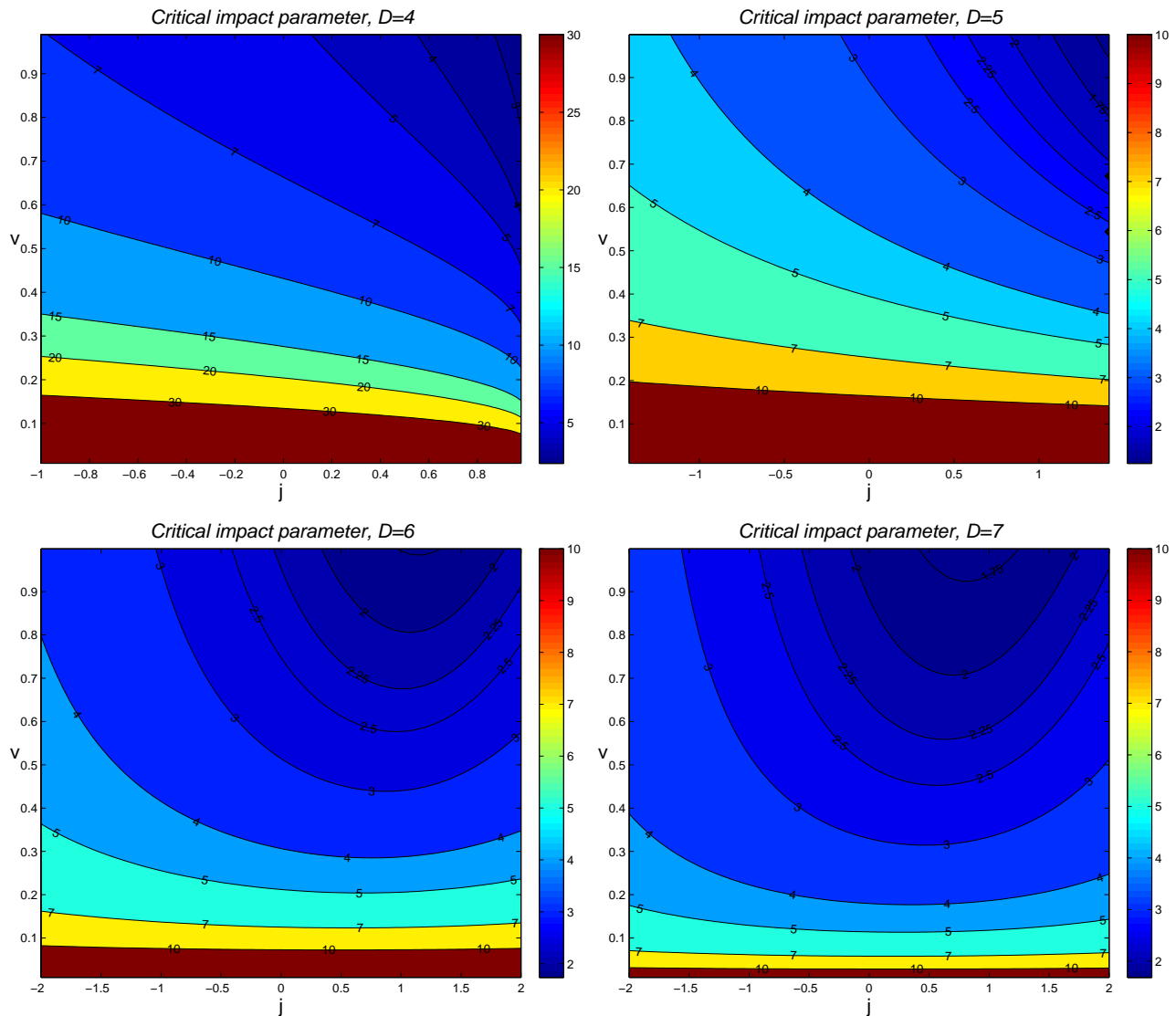


FIG. 4: Contour plots of the critical impact parameter in the (v, j) plane for corotating orbits ($j > 0$) and counterrotating orbits ($j < 0$) in dimensions $D = 4$, $D = 5$, $D = 6$ and $D = 7$.

III. THE ZFL IN GRAZING COLLISIONS

In this section we generalize the classic ZFL calculations for head-on collisions [20, 21] to the case of collisions with finite impact parameter. The initial configuration consists of two point particles with mass M_k freely moving toward each other with constant, positive velocity v_k , corresponding to boost factors $E_k = (1 - v_k^2)^{-1/2}$ ($k = 1, 2$). For convenience the axes are oriented such that the initial motion is in the x -direction (see Fig. 5). We assume that at $x = 0$ the particles “collide” with generic impact parameter b and form a single final body (strictly speaking this assumption is only valid for small impact parameters, because we expect the bodies to scatter when b is large enough). Since the collision is not head-on (and since the energy loss is not included in

the motion of point particles), some confining force is necessary to bind the particles. In fact, we show below that additional “stresses” are required to guarantee energy conservation (cf. Ref. [37]).

Before the collision the particles have four-positions and four-momenta given by:

$$\begin{aligned} x_1^\mu &= (t, v_1 t, \xi_1, 0), & x_2^\mu &= (t, -v_2 t, -\xi_2, 0), \\ p_1^\mu &= E_1 M_1 (1, v_1, 0, 0), & p_2^\mu &= E_2 M_2 (1, -v_2, 0, 0), \end{aligned} \quad (21)$$

where ξ_1 ($-\xi_2$) is the projection of the position of particle 1 (2) along the y -axis before the collision. If the system’s center of mass is at $y = 0$, the position of particle 2 before the collision can also be written as $y = -(b - \xi_1) \equiv -\xi_2$, where b is the impact parameter.

At $t = 0$ the particles become constrained to move as if they were attached to an infinitesimally thin, massless

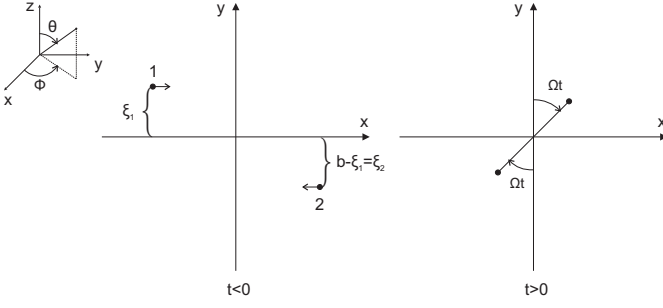


FIG. 5: The system before and after the collision. ξ_1 is defined in Eq. (22).

rod of length b . This fictional rod is an idealization, but it is necessary to guarantee energy-momentum conservation. For $t > 0$ the particles remain attached to the rod, so that (in the center-of-momentum frame) they rotate around the origin at fixed separation b . Using primes to denote final states, the four-positions and four-momenta after the collision are:

$$\begin{aligned} (x_1^\mu)' &= (t, \xi_1 S, \xi_1 C, 0), \\ (x_2^\mu)' &= (t, -\xi_2 S, -\xi_2 C, 0), \\ (p_1^\mu)' &= E_1 M_1 (1, \xi_1 \Omega C, -\xi_1 \Omega S, 0), \\ (p_2^\mu)' &= E_2 M_2 (1, -\xi_2 \Omega C, \xi_2 \Omega S, 0), \end{aligned}$$

where $S \equiv \sin(\Omega t)$, $C \equiv \cos(\Omega t)$.

A few relations can be derived between (ξ_1, ξ_2) and (v_1, v_2) due to the constraints we imposed. The requirement that the system's center of mass is at $y = 0$ implies

$$\xi_1 = \frac{b E_2 M_2}{E_1 M_1 + E_2 M_2}. \quad (22)$$

In the center-of-momentum frame we also have

$$E_1 M_1 v_1 = E_2 M_2 v_2. \quad (23)$$

For an instantaneous collision the energy-momentum tensor of the system is given by:

$$\begin{aligned} T^{\mu\nu}(\mathbf{x}, t) &= \sum_{k=1}^2 \frac{p_k^\mu p_k^\nu}{E_k M_k} \delta^3(\mathbf{x} - \mathbf{x}_k(t)) \Theta(-t) \\ &+ \sum_{k=1}^2 \frac{(p_k^\mu)'(t) (p_k^\nu)'(t)}{E_k M_k} \delta^3(\mathbf{x} - \mathbf{x}'_k(t)) \Theta(t), \end{aligned} \quad (24)$$

where the boldface denotes a three-vector, and the angular momentum is

$$\begin{aligned} S_3 &= \int (x^1 T^{20} - x^2 T^{10}) d^3 \mathbf{x} \\ &= - \sum_{k=1}^2 [\Theta(-t) E_k M_k v_k \xi_k + \Theta(t) E_k M_k \Omega \xi_k^2]. \end{aligned} \quad (25)$$

Angular momentum conservation implies that the rotation frequency must be

$$\Omega = \frac{E_1 M_1 v_1 \xi_1 + E_2 M_2 v_2 \xi_2}{E_1 M_1 \xi_1^2 + E_2 M_2 \xi_2^2}. \quad (26)$$

If we naively take the stress-energy tensor of Eq. (24) to be the full energy-momentum of the system, we would find that it is not covariantly conserved, i.e. $\nabla_\mu T^{\mu\nu} = 0$ for $\nu = t, z$ but $\nabla_\mu T^{\mu\nu} \neq 0$ for $\nu = x, y$. In fact, one finds (in the center-of-momentum frame)

$$\begin{aligned} \nabla_\mu T^{\mu x} &= -E_1 M_1 \xi_1 \Omega^2 S \delta(x - \xi_1 S) \delta(y - \xi_1 C) \delta(z) \Theta(t) \\ &+ E_2 M_2 \xi_2 \Omega^2 S \delta(x + \xi_2 S) \delta(y + \xi_2 C) \delta(z) \Theta(t), \\ \nabla_\mu T^{\mu y} &= -E_1 M_1 \xi_1 \Omega^2 C \delta(x - \xi_1 S) \delta(y - \xi_1 C) \delta(z) \Theta(t) \\ &+ E_2 M_2 \xi_2 \Omega^2 C \delta(x + \xi_2 S) \delta(y + \xi_2 C) \delta(z) \Theta(t). \end{aligned}$$

Physically, this nonconservation of stress-energy is due to neglecting the energy-momentum associated with the fictitious rod that keeps the particles in circular orbit.

Energy-momentum conservation can be enforced by adding an additional term for each particle that represents this constraining force. The contribution of such forces to the gravitational radiation emitted by a particle in circular orbit was studied by Price and Sandberg [37]. By adding a radial tension $\tau_k(r)$ for each particle and imposing that $\nabla_\mu T^{\mu\nu} = 0$ we get the following contributions to the energy-momentum tensor:

$$\begin{aligned} T_{\text{tens}}^{xx}(t, \mathbf{x}) &= -S^2 \delta(\cos \theta) \Theta(t) \sum_{k=1}^2 \tau_k(r) \delta(\phi + \Omega t - \phi_k), \\ T_{\text{tens}}^{yy}(t, \mathbf{x}) &= -C^2 \delta(\cos \theta) \Theta(t) \sum_{k=1}^2 \tau_k(r) \delta(\phi + \Omega t - \phi_k), \\ T_{\text{tens}}^{xy}(t, \mathbf{x}) &= -SC \delta(\cos \theta) \Theta(t) \sum_{k=1}^2 \tau_k(r) \delta(\phi + \Omega t - \phi_k), \end{aligned}$$

where $\phi_1 = \pi/2$, $\phi_2 = 3\pi/2$ and

$$\tau_k(r) = \frac{M_k \xi_k \Omega^2 \Theta(\xi_k - r)}{r^2 \sqrt{1 - (\xi_k \Omega)^2}}, \quad (k = 1, 2). \quad (27)$$

Here $r = \sqrt{x^2 + y^2 + z^2}$, θ is the polar angle measured from the positive z -axis, and ϕ is the azimuthal angle in the x - y plane measured from the x -axis (see Fig. 5).

The factor $[1 - (\xi_k \Omega)^2]^{-1/2}$ is just the boost factor for particle k in circular motion with angular frequency Ω . The stresses vanish for $b = 0$, as one would expect.

A. Equal-mass collisions

In this subsection we study the equal-mass case $M/2 \equiv M_1 = M_2$, where M is the total mass, and $v_1 = v_2 = v$, $E_1 = E_2 = E$. According to Eq. (26), after the collision the particles are on a bound circular orbit with radius $b/2$ and rotational frequency $\Omega = 2v/b$. The Fourier transform of the energy-momentum tensor (24) yields

$$T^{\mu\nu}(\mathbf{k}, \omega) = \frac{p_1^\mu p_1^\nu}{2\pi i E_1 M_1 (\omega - v_1 k_x)} e^{-ik_y b/2} + \frac{p_2^\mu p_2^\nu}{2\pi i E_2 M_2 (\omega + v_2 k_x)} e^{ik_y b/2} + \sum_{k=1}^2 \int_{-\infty}^{\infty} \frac{p_k'^\mu(t) p_k'^\nu(t)}{2\pi E_k M_k} \exp(i\omega t - i\mathbf{k} \cdot \mathbf{x}'_k(t)) \Theta(t) dt + \frac{1}{2\pi} \int d^4x T_{\text{tens}}^{\mu\nu}(\mathbf{x}, t) e^{i\omega t - i\mathbf{k} \cdot \mathbf{x}}, \quad (28)$$

where $d^4x = dx dy dz dt$ and \mathbf{k} is the wave vector:

$$k_x = \omega \sin \phi \cos \theta, \quad k_y = \omega \sin \phi \sin \theta, \quad k_z = \omega \cos \phi. \quad (29)$$

We also have

$$e^{i\omega t - i\mathbf{k} \cdot \mathbf{x}'_k(t)} = e^{i\omega t} \exp\left(i\lambda_k \frac{\omega b}{2} \sin \theta \sin(\Omega t + \phi)\right), \quad (30)$$

where $k = 1, 2$ is the particle index, $\lambda_1 = -1$ and $\lambda_2 = 1$. If we set $\alpha = \Omega t + \phi$ and $2\eta_k = \lambda_k \omega b \sin \theta$ the last exponential can be written in terms of Bessel functions of the first kind, using the Jacobi-Anger expansion [42]:

$$e^{i\eta \sin \alpha} = \sum_{n=-\infty}^{n=+\infty} J_n(\eta) e^{in\alpha}. \quad (31)$$

For large n the Bessel functions satisfy [42]

$$J_n(\eta) \sim \frac{1}{\sqrt{2\pi n}} \left(\frac{e\eta}{2n}\right)^n. \quad (32)$$

A time-integration introduces an additional factor of $1/n$, so the series converges rapidly for large $|n|$ and we can truncate it at some moderately large value of $n = N$ to get an accurate approximation of the integral¹. Typically, $N \gtrsim 10$ is sufficient for an accuracy of 1% or better.

The integration of the stresses proceeds in a similar way. After integrating in θ and ϕ , the same Bessel function expansion can be used for the time-integration. The integral of Bessel functions with respect to r can be evaluated using the following identity [42]:

$$\int_0^\eta J_\nu(r) dr = 2 \sum_{k=0}^{\infty} J_{\nu+2k+1}(\eta), \quad \text{Re}(\nu) > -1. \quad (33)$$

¹ Actually, the series should be approximated by summing from $n = n_0 - N$ to $n = n_0 + N$, where n_0 is the value of n which maximizes the absolute value of the terms being summed. After the integration terms of the form $1/(\omega - n\Omega)$ appear. This means that the largest contribution to the sum corresponds to some $n_0 \neq 0$. However it can be checked that $N \gg n_0$ for the range of parameters considered here, so the sum can be taken in a symmetric interval around 0.

1. Radiation Spectrum

The energy per solid angle and per unit frequency emitted in the direction $\hat{\mathbf{k}} = \mathbf{k}/\omega$ is [43]:

$$\frac{d^2 E}{d\omega d\Omega} = 2\omega^2 \left(T^{\mu\nu}(\mathbf{k}, \omega) T_{\mu\nu}^*(\mathbf{k}, \omega) - \frac{1}{2} |T^\lambda{}_\lambda(\mathbf{k}, \omega)|^2 \right), \quad (34)$$

where the asterisk stands for complex conjugation. The energy can also be expressed in terms of the purely space-like components of $T^{\mu\nu}$. The conservation equation for $T^{\mu\nu}$ implies that $k_\mu T^{\mu\nu}(\mathbf{k}, \omega) = 0$, so it is possible to write T^{00} and T^{0i} in terms of T^{ij} :

$$T_{00}(\mathbf{k}, \omega) = \hat{k}^i \hat{k}^j T_{ij}(\mathbf{k}, \omega), \quad (35)$$

$$T_{0i}(\mathbf{k}, \omega) = -\hat{k}^j T_{ij}(\mathbf{k}, \omega). \quad (36)$$

With these identities at hand, Eq. (34) can be written as:

$$\frac{d^2 E}{d\omega d\Omega} = 2\omega^2 \Lambda_{ijklm}(\hat{k}) T^{*ij}(\mathbf{k}, \omega) T^{lm}(\mathbf{k}, \omega), \quad (37)$$

where following Ref. [43] we defined

$$\Lambda_{ijklm}(\hat{k}) = \delta_{il} \delta_{jm} - 2\hat{k}_j \hat{k}_m \delta_{il} + \frac{1}{2} \hat{k}_i \hat{k}_j \hat{k}_l \hat{k}_m - \frac{1}{2} \delta_{ij} \delta_{lm} + \frac{1}{2} \delta_{ij} \hat{k}_l \hat{k}_m + \frac{1}{2} \delta_{lm} \hat{k}_i \hat{k}_j. \quad (38)$$

In Fig. 6 we plot the energy spectrum for $E = 3$ along four different directions: $\hat{\mathbf{k}} = \mathbf{e}_x, \mathbf{e}_y, \mathbf{e}_z, (\mathbf{e}_x + \mathbf{e}_y + \sqrt{2}\mathbf{e}_z)/2$. For dimensional reasons, there is no need to fix b as long as the energy is plotted as a function of ω/Ω . All spectra diverge when $\omega = 2\Omega$, as expected of a rigid symmetric body rotating with angular frequency Ω . For $\hat{\mathbf{k}} = \mathbf{e}_z$ the spectrum only diverges at $\omega = 2\Omega$ (see Ref. [44] for a discussion of particles in circular orbit in the Schwarzschild geometry), but in all other directions the spectrum diverges at even multiples of the rotational frequency Ω . The same qualitative features hold for higher boost parameters.

2. Head-on collisions

Let us consider the $b = 0$ limit, which corresponds to a head-on collision and for which we can compare against

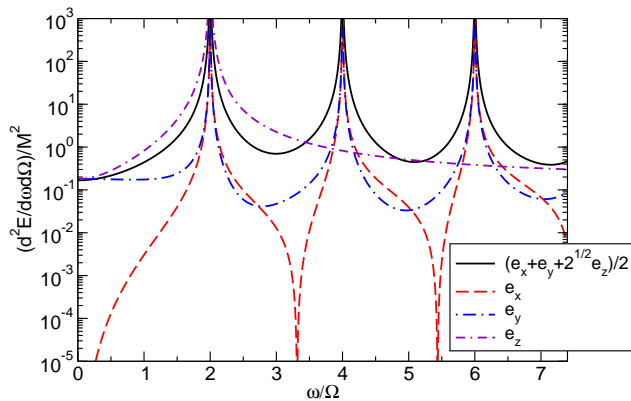


FIG. 6: Energy per unit solid angle and per unit frequency emitted in the directions $\hat{\mathbf{k}} = \mathbf{e}_x, \mathbf{e}_y, \mathbf{e}_z, (\mathbf{e}_x + \mathbf{e}_y + \sqrt{2}\mathbf{e}_z)/2$ by equal-mass binaries with $E = 3$, as a function of ω/Ω .

known results [20, 21]. In this limit, the only nonvanishing components of the energy-momentum tensor are:

$$\begin{aligned} 2\pi\omega T^{tt}(\mathbf{k}, \omega) &= iEM - \frac{iEM}{1 - v^2 \sin^2 \theta \cos^2 \phi}, \\ 2\pi\omega T^{tx}(\mathbf{k}, \omega) &= -\frac{iEMv^2 \sin \theta \cos \phi}{1 - v^2 \sin^2 \theta \cos^2 \phi}, \\ 2\pi\omega T^{xx}(\mathbf{k}, \omega) &= -\frac{iEMv^2}{1 - v^2 \sin^2 \theta \cos^2 \phi}. \end{aligned}$$

The energy spectrum per unit solid angle is then given by

$$\frac{d^2 E}{d\omega d\Omega} = \frac{E^2 M^2 v^4 (\sin^2 \theta \cos^2 \phi - 1)^2}{4\pi^2 (v^2 \sin^2 \theta \cos^2 \phi - 1)^2}. \quad (39)$$

This agrees with previous results in the literature. Indeed, after a trivial redefinition of angles, Eq. (39) is equal to Eqs. (2.19) and (2.12) of Refs. [20] and [21], respectively. In Refs. [20, 21] the angular variable θ is the angle between the radiation direction and the momenta of the particles; the substitution of their $\cos \theta$ by $\sin \theta \cos \phi$ yields Eq. (39). For ease of comparison with NR results [4, 6], it is convenient to expand the above expression in spin-weighted spherical harmonics with spin weight $s = -2$. Such an expansion is discussed in Appendix B.

Recalling that \mathbf{e}_x corresponds to $(\theta = \pi/2, \phi = 0)$, \mathbf{e}_y corresponds to $(\theta = \pi/2, \phi = \pi/2)$ and \mathbf{e}_z corresponds to $\theta = 0$ we get:

$$\frac{d^2 E}{d\omega d\Omega} = 0 \quad \text{along } \mathbf{e}_x, \quad (40a)$$

$$\frac{d^2 E}{d\omega d\Omega} = \frac{E^2 M^2 v^4}{4\pi^2} \quad \text{along } \mathbf{e}_y, \mathbf{e}_z. \quad (40b)$$

The radiated momentum per unit frequency for this head-on collision is found by the following integral over

a two-sphere at infinity, S_∞ , centered on the coordinate origin:

$$\frac{dP_i}{d\omega} = \int_{S_\infty} \frac{d^2 E}{d\omega d\Omega} n_i d\Omega, \quad (41)$$

where n_i is a unit radial vector normal to S_∞ . In the present case we find that the radiated momentum vanishes, i.e. $dP_i/d\omega = 0$, as one would expect.

3. Zero-frequency limit

For arbitrary impact parameters our results show that, in the limit $b\omega \rightarrow 0$, the energy spectrum is independent of b and given by Eq. (39). This is of course consistent with the head-on results of Smarr [20] and Adler and Zeks [21]. Numerical calculations support this conclusion and reveal additional details for small but nonzero frequencies. The stress terms give the following contributions to the energy-momentum tensor:

$$\begin{aligned} \omega T_{\text{tens}}^{xx}(\mathbf{k}, \omega) \Big|_{\omega=0} &= \omega T_{\text{tens}}^{yy}(\mathbf{k}, \omega) \Big|_{\omega=0} = -\frac{ib^2 EM \Omega^2}{16\pi}, \\ \omega T_{\text{tens}}^{xy}(\mathbf{k}, \omega) \Big|_{\omega=0} &= 0. \end{aligned} \quad (42)$$

For $\omega = 0$ the constraining forces provide a nonvanishing contribution to the energy-momentum tensor. It is this particular contribution that allows one to recover the ZFL of the energy spectrum, Eq. (39), for *any* impact parameter. This is one of the most intriguing results of this incursion into the properties of the ZFL for collisions with nonzero impact parameter.

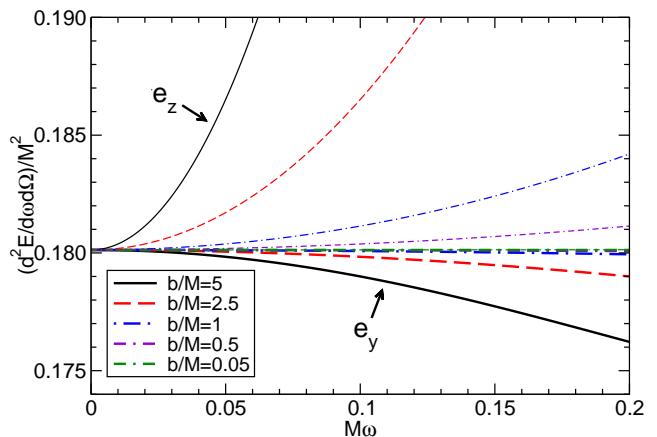


FIG. 7: Normalized energy spectrum per unit solid angle emitted in the directions $\hat{\mathbf{k}} = \mathbf{e}_y$ (thick lines) and $\hat{\mathbf{k}} = \mathbf{e}_z$ (thin lines) as a function of $M\omega$ for several values of b/M (as indicated in the legend) and $E = 3$. As indicated by Eq. (40) the ZFL for these two different directions is the same and approximately equal to $0.18013M^2$.

The spectra for small frequencies along the directions $\hat{\mathbf{k}} = \mathbf{e}_y$ and $\hat{\mathbf{k}} = \mathbf{e}_z$ are plotted in Fig. 7 for different values of b/M . All spectra have the same ZFL, as discussed

above. Specializing Eq. (40b) to the case $E = 3$ we get $\frac{d^2 E}{d\omega d\Omega}\Big|_{\omega=0} = 0.18013M^2$ for $\mathbf{e}_y, \mathbf{e}_z$. This is in very good agreement with the numerical results shown in Fig. 7.

For small but finite frequencies, we find that the slope

$$\begin{aligned} \frac{d^2 E}{d\omega d\Omega} &= \frac{E^2 M^2 v^2}{16\pi^2 (1 - v^2 \sin^2 \theta \cos^2 \phi)^2} \left\{ 4v^2 (\sin^2 \theta \cos^2 \phi - 1)^2 - \right. \\ &\quad - \frac{1}{6} \left[v^2 (8v^2 + 3) \sin^6 \theta \cos^4 \phi + \sin^2 \theta ((8v^2 + 3) \cos 2\phi + 12(v^2 + 1)) - \right. \\ &\quad \left. \left. - \sin^4 \theta \cos^2 \phi (6v^4 + (2v^2 + 3)v^2 \cos 2\phi + 20v^2 + 3) - 12 \right] (b\omega)^2 \right\} + \mathcal{O}[(b\omega)^3]. \end{aligned} \quad (43)$$

Thus, within our model the spectrum typically has quadratic corrections, except along $\hat{\mathbf{k}} = \mathbf{e}_x$, in which case the first nonvanishing contribution to the energy spectrum is of order $(b\omega)^4$. In fact, we find

$$\frac{d^2 E}{d\omega d\Omega}\Big|_{\hat{\mathbf{k}}=\mathbf{e}_x} = -\frac{E^2 M^2 (3 - 2v^2)^2}{9216\pi^2} (b\omega)^4 + \mathcal{O}[(b\omega)^5]. \quad (44)$$

These analytical expressions are in good agreement with the results shown in Fig. 7.

B. Extreme-mass ratio collisions

We now study collisions for $\mu \equiv M_1 \ll M_2 \equiv M$ (the qualitative features of the radiation for *generic* mass ratio are very similar to the extreme-mass ratio case). The energy spectrum can be computed in the center-of-momentum frame. Since particle 2 is much heavier than particle 1, particle 2 is practically at rest in this frame, although we shall not neglect its motion when we compute the energy-momentum tensor. Therefore, we let $v_1 \equiv v \gg v_2$ and $E_1 \equiv E$.

From Eqs. (22) and (26), the angular frequency and position of particle 1 are given by

$$\Omega = \frac{E_1 \mu v_1 \xi_1 + E_2 M v_2 \xi_2}{E_1 \mu \xi_1 + E_2 M \xi_2}, \quad \xi_1 = \frac{b E_2 M}{E_1 \mu + E_2 M}. \quad (45)$$

Once again we must add the stresses needed to constrain the particles in their orbits, in order to have a conserved energy-momentum tensor.

1. Radiation Spectrum

We compute the radiated energy using Eq. (34) or Eq. (37). We expand the energy-momentum tensor in powers of μ/M , and compute the energy keeping only leading-order contributions in μ/M . A calculation of the

of the energy spectrum depends on direction. It is positive (negative) for $\hat{\mathbf{k}} = \mathbf{e}_y$ (\mathbf{e}_z , respectively), and it increases with b/M . An expansion of the energy for small $b\omega$ yields

radiation for $E = 3$ (in the center-of-momentum frame) along several different directions yields the spectra shown in Fig. 8.

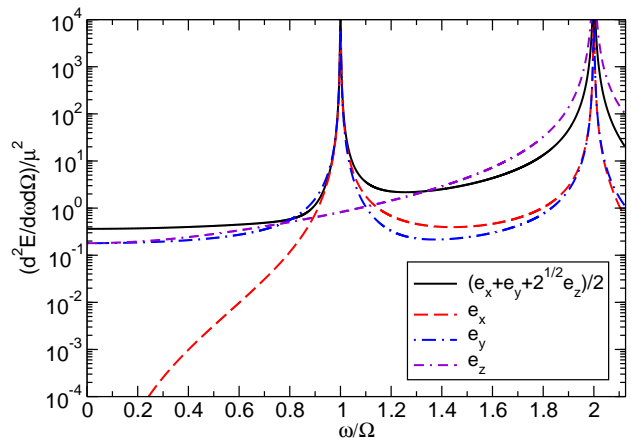


FIG. 8: Normalized energy spectrum per solid angle emitted in the directions $\hat{\mathbf{k}} = \mathbf{e}_x, \mathbf{e}_y, \mathbf{e}_z, (\mathbf{e}_x + \mathbf{e}_y + \sqrt{2}\mathbf{e}_z)/2$ as a function of ω/Ω in the extreme-mass ratio case.

The extreme-mass ratio configuration loses the angular symmetry of the equal-mass case. Therefore, the spectra now diverge for all multiples of Ω for $\hat{\mathbf{k}} = \mathbf{e}_x, \hat{\mathbf{k}} = \mathbf{e}_y$. The behavior is similar for other directions. For $\hat{\mathbf{k}} = \mathbf{e}_z$, the spectrum only diverges for $\omega = 2\Omega$, in agreement with Poisson's findings for particles in circular orbit around BHs [44].

2. Head-on collisions

For extreme-mass ratio head-on collisions ($b = 0$) we find

$$\frac{d^2 E}{d\omega d\Omega} = \frac{E^2 \mu^2 v^4 (\sin^2 \theta \cos^2 \phi - 1)^2}{4\pi^2 (v \sin \theta \cos \phi - 1)^2}. \quad (46)$$

This expression coincides, as it should, with Eq. (2.17) of Smarr [20], once we take into account the different convention on angles by an appropriate redefinition of angular variables (cf. the discussion following Eq. (39).) For ease of comparison with perturbative results of point particles in BH spacetimes, in Appendix B we compute analytically the multipolar decomposition of this ZFL result in spin-weighted spherical harmonics.

By computing the radiated momentum using Eq. (41) we find that it vanishes along the y - and z -axes, and that along the x -axis it is given by

$$\frac{dP^x}{d\omega} = \frac{\mu^2 E^2 [v(15 - 13v^2) - 3(v^4 - 6v^2 + 5) \operatorname{arctanh} v]}{3\pi v^2}. \quad (47)$$

This result is in good agreement with the linear momen-

tum radiated by point particles falling into Schwarzschild BHs, as we will see in section IV D.

3. Zero-frequency limit

Let us now consider the ZFL for generic values of the impact parameter. As $b\omega \rightarrow 0$ we find once again that the energy spectrum is independent of the impact parameter (as it was for the equal-mass collisions of section III A). The leading-order expression of the energy in powers of μ/M is given by Eq. (46), reproducing Smarr's result for head-on collisions. Including higher powers of $b\omega$ we get

$$\begin{aligned} \frac{d^2 E}{d\omega d\Omega} &= \frac{E^2 \mu^2 v^2}{4\pi^2 (v \sin \theta \cos \phi - 1)^2} \left\{ v^2 (\sin^2 \theta \cos^2 \phi - 1)^2 - \right. \\ &- \frac{1}{192} \left[(-4v(2v^2 + 3) \sin^3 \theta (\cos 2\theta + 3) \cos 3\phi + 8 \sin^2 \theta \cos 2\phi ((3 - 10v^2) \cos 2\theta - 6v^2 + 9) + \right. \\ &+ v \sin \theta \cos \phi ((372 - 8v^2) \cos 2\theta + (6v^2 + 9) \cos 4\theta + 2v^2 + 387) + 8(2v^2 - 21) \cos 2\theta + \\ &\left. \left. + (20v^2 - 6) \cos 4\theta - 6(6v^2 + 35) \right] (b\omega)^2 \right\} + \mathcal{O}[(b\omega)^3]. \end{aligned} \quad (48)$$

As in the equal-mass case, here too the radiation is suppressed along the x -axis, where the leading contribution is of order $(b\omega)^4$:

$$\left. \frac{d^2 E}{d\omega d\Omega} \right|_{\hat{k}=\mathbf{e}_x} = \frac{E^2 \mu^2 (3 - 2v(v + 3))^2}{576\pi^2} (b\omega)^4 + \mathcal{O}[(b\omega)^5]. \quad (49)$$

C. Generality of the model

The most important result of our ZFL calculation for collisions with generic impact parameter is perhaps that the ZFL itself is *independent* of the impact parameter. One of the limitations of the present calculation is that the modeling of the collision is rather ad-hoc, especially in the specification of the nature of the constraining forces. It is natural to ask how the results would change if the constraining forces were modeled differently. For example, in our toy model the final system consists of two particles bound in a circular orbit, so the radiation spectrum shows peaks typical of the radiation produced by rotating bodies. There is a chance that the divergence at harmonics of the rotational frequency of the final system could contaminate the low-frequency behavior of the spectrum.

To investigate this possibility, instead of considering the collision of two point particles, we studied a point

particle colliding with a special extended matter distribution: specifically, we considered an infinitely thin, slowly rotating, uniform disk. For brevity we do not report details of this calculation here. Our main finding is that, if the disk is initially slowly rotating (so that after the collision the system is at rest), the ZFL is the *same* as in the case of two colliding particles. This is by no means a proof that the ZFL is completely independent of the way one models the system. It is however a hint that (as physical intuition would suggest) the ZFL should depend only on the asymptotic momenta of the colliding particles.

IV. ULTRARELATIVISTIC INFALL OF POINT PARTICLES

The formalism discussed in section III is a flat-space approximation valid for the low-frequency part of the energy spectrum and of the gravitational waveforms. In this section we compute the radiation from the linearized field equations in the *curved* background of a Schwarzschild BH. This is an accurate description at all frequencies in the limit where one of the binary components is much more massive than the other.

There is extensive literature on the gravitational radiation emitted by particles following geodesics in BH backgrounds (see [45] and Appendix C of [46] for summaries).

Here we present an incomplete overview of this literature. Davis *et al.* first studied the radiation emitted by particles falling radially from rest into a Schwarzschild BH [47] and the synchrotron radiation emitted by particles in circular orbits [48] (see also [49] and Detweiler’s contribution to Ref. [50]). Oohara and Nakamura computed the energy, angular momentum and linear momentum radiated by particles falling from rest with generic angular momentum into Schwarzschild BHs [51, 52]. This work was later generalized to particles on *scattering* orbits in Schwarzschild, starting either from rest [53] or with finite energy at infinity [54]. Radial infalls into a nonrotating BH with finite energy were considered in Refs. [22–24], and the ultrarelativistic limit was compared with Smarr’s ZFL in Refs. [25–27] (in four dimensions) and [28] (in dimensions $D \geq 4$). Oohara, Kojima and Nakamura studied orbits plunging [51, 55–57] and scattering [58] from rest in the case of rotating (Kerr) BHs. More recent studies focused on the threshold of immediate merger using the geodesic analogy [13–16].

Perhaps because of the limited astrophysical relevance of infalls with finite energy at infinity, to our knowledge there is no detailed study of the radiation emitted by point particles falling with generic energy and impact parameter into Schwarzschild BHs. One purpose of this section is to fill this surprising gap in the literature. A complementary study of scattering orbits with generic energy can be found in Ref. [54]. The generalization of this study to particles falling with arbitrary energy and impact parameter into Kerr BHs is in preparation.

The radiation can be determined from the knowledge of the Sasaki-Nakamura wave function X_{lm} , which (in the frequency domain) can be written in the form

$$\frac{d^2 X_{lm}}{dr_*^2} + \left[\omega^2 - \frac{\Delta}{r^5} (l(l+1)r - 6M) \right] X_{lm} = S_{lm}. \quad (50)$$

Here (l, m) are (tensor) spherical harmonic indices resulting from a separation of the angular variables, ω is the Fourier frequency of the perturbation and $\Delta \equiv r(r-2M)$. The boundary conditions dictate that we should have outgoing waves at infinity and ingoing waves at the BH horizon:

$$X_{lm} = \begin{cases} X_{lm}^{\text{in}} e^{-i\omega r_*}, & r_* \rightarrow -\infty, \\ X_{lm}^{\text{out}} e^{i\omega r_*}, & r_* \rightarrow +\infty. \end{cases} \quad (51)$$

The source term S_{lm} in the Sasaki-Nakamura equation (50) is determined by the point-particle trajectory. Without loss of generality we assume the trajectory to be an “equatorial” ($\theta = \pi/2$) timelike geodesic in the Schwarzschild background, parametrized by

$$R^2 \dot{R}^2 = R^2(E^2 - 1) - f(R) L_z^2 + 2MR, \quad (52)$$

$$R^2 \dot{\phi} = L_z, \quad f(R) \dot{T} = E, \quad (53)$$

where $f(R) = 1 - 2M/R$ and dots stand for derivatives with respect to proper time τ . As usual we denote by L_z the orbital angular momentum of the particle along the

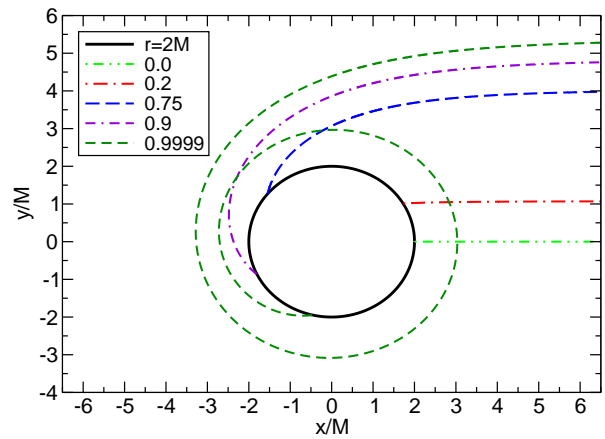


FIG. 9: Trajectories for different values of L_z/L_{crit} (as indicated in the legend) and $E = 3$. The black circle of radius 2 marks the location of the horizon.

z -axis and by E the particle’s energy at infinity per unit mass μ , so $E = 1$ corresponds to an infall from rest. We remind the reader that the impact parameter b is related to L_z by $b \equiv L_z/\sqrt{E^2 - 1}$. The geodesic equations can be integrated numerically for chosen values of E and L_z . For $L_z > L_{\text{crit}} = L_{\text{crit}}(E)$ (see section II A) the particle does not plunge, but rather scatters to infinity. We restrict our discussion to the case $L < L_{\text{crit}}$. Examples of plunging orbits for $E = 3$ and different angular momenta (i.e., different impact parameters) are shown in Fig. 9.

Given a particle trajectory, the numerical calculation of the gravitational radiation emitted by the system involves the solution of Eq. (50), which can be obtained by the standard Green’s function technique (more details on the formalism can be found in Appendix A). Omitting for simplicity the indices (l, m) , we first define two independent solutions $X_{\text{in}}^{(0)}, X_{\text{out}}^{(0)}$ with boundary conditions

$$X_{\text{in}}^{(0)} = \begin{cases} e^{-i\omega r_*}, & r_* \rightarrow -\infty, \\ A_{\text{out}} e^{i\omega r_*} + A_{\text{in}} e^{-i\omega r_*}, & r_* \rightarrow +\infty. \end{cases} \quad (54a)$$

$$X_{\text{out}}^{(0)} = \begin{cases} B_{\text{out}} e^{i\omega r_*} + B_{\text{in}} e^{-i\omega r_*}, & r_* \rightarrow -\infty, \\ e^{i\omega r_*}, & r_* \rightarrow +\infty, \end{cases} \quad (54b)$$

Then the solution of the inhomogeneous Sasaki-Nakamura equation (50) is given by

$$X_{lm} = \frac{1}{W} \left[X_{\text{in}}^{(0)} \int_{r_*}^{\infty} S_{lm} X_{\text{out}}^{(0)} dr_* + X_{\text{out}}^{(0)} \int_{-\infty}^{r_*} S_{lm} X_{\text{in}}^{(0)} dr_* \right]. \quad (55)$$

where $W \equiv 2i\omega A_{\text{in}}$ is the Wronskian. Asymptotically for $r_* \rightarrow \infty$ the amplitude of the wave function is

$$X_{lm}^{\text{out}} = \frac{1}{W} \int_{-\infty}^{\infty} S_{lm} X_{\text{in}}^{(0)} dr_*. \quad (56)$$

Then the radiated energy, angular momentum and linear

momentum are given by the multipolar sums

$$E^{\text{rad}} = \int_0^\infty d\omega \sum_{lm} \frac{dE_{lm}}{d\omega}, \quad (57)$$

$$J^{\text{rad}} = \int_0^\infty d\omega \sum_{lm} \frac{m}{\omega} \frac{dE_{lm}}{d\omega}, \quad (58)$$

$$P_x + iP_y = \int_0^\infty d\omega 16\omega^2 \sum_{lm} \left[q_{lm} X_{l,m}^{\text{out}} \bar{X}_{l,m+1}^{\text{out}} + p_{lm} (X_{l,m}^{\text{out}} \bar{X}_{l+1,m+1}^{\text{out}} - \bar{X}_{l,-m}^{\text{out}} X_{l+1,-m-1}^{\text{out}}) \right], \quad (59)$$

with

$$\begin{aligned} \frac{dE_{lm}}{d\omega} &= 16\omega^2 |X_{lm}^{\text{out}}|^2, \\ p_{lm} &= \left[\frac{(l+3)(l-1)(l+m+2)(l+m+1)}{(2l+3)(2l+1)(l+1)^2} \right]^{1/2}, \\ q_{lm} &= -2 \frac{\sqrt{(l-m)(l+m+1)}}{l(l+1)}. \end{aligned} \quad (60)$$

Note that the radiated momentum in the z -direction $P_z = 0$ by symmetry. Details on the derivation of the source term and asymptotic expansions of the wave functions which are necessary to improve the numerical accuracy of the Wronskian are given in Appendix A.

We integrate all differential equations in C++ using the adaptive stepsize integrator STEPPERDOPR5 [59]. Schematically, the integration consists of the following steps: (i) integrate the first independent solution of the homogeneous SN equation (50) with the boundary conditions (54a) from $r_h = 2M(1 + \delta r)$ outwards (typically we choose $\delta r = 10^{-4}$); (ii) integrate the second independent solution of the homogeneous equation with boundary conditions (54b) from $r_\infty = r_\infty^{(0)}/\omega$ inwards, where typically we choose $r_\infty^{(0)} = 4 \times 10^4$; (iii) compute the Wronskian at the large but finite radius $r_\infty^{(0)}$, using Eq. (A29) for increased accuracy; (iv) integrate the geodesics with given orbital parameters and at the same time compute the source term using Eqs. (A20) and (A23); (v) output the “in” solution $X_{\text{in}}^{(0)}$ and the source term S_{lm} on a grid of $n = 1.6 \times 10^5$ colocation points, and use a Gauss-Legendre spectral integrator [59] to compute the convolution of the homogeneous solutions with the source term entering the expression for the outgoing amplitude X_{lm}^{out} , Eq. (56); (vi) sum over multipoles to get the total radiated energy (57), the angular momentum (58) and the linear momentum in the x - and y -directions (59).

In the remainder of this section we summarize the results obtained by this procedure.

A. Point-particle spectra

We performed an extensive set of simulations, selecting seven values of the normalized particle energies ($E =$

1, 1.5, 3, 5, 10, 20, 100). For each value of E we considered nine different particle angular momenta ($L_z/L_{\text{crit}} = 0, 0.2, 0.5, 0.75, 0.9, 0.95, 0.99, 0.999, 0.9999$), for a total of 63 different configurations. We also ran a few more cases to validate our code against the results of Ref. [51]. Our results are in good visual agreement with their plots. For each of the 63 simulations we computed all multipolar components of the radiation up to $l = l_{\text{max}} = 6$ for $10^{-2} \leq \omega \leq 1.5$ in steps of $\delta\omega = 10^{-2}$; in a few selected cases we ran the code up to $l = l_{\text{max}} = 8$ to check the convergence of the results against truncation of the multipolar sum. We also verified that for head-on collisions with $E > 1$ our results are in agreement (within three decimal places) with Table II of Ref. [24].

For each value of l , most of the radiation is typically emitted in the $l = m$ component. In Fig. 10 we show the $l = m$ component of the energy spectra for particles falling from rest ($E = 1$) and for kinetic-energy dominated infalls ($E = 3$). In each of these two cases we plot the spectra for three selected values of the angular momentum: $L_z/L_{\text{crit}} = 0$ (a head-on infall), $L_z/L_{\text{crit}} = 0.9$ and $L_z/L_{\text{crit}} = 0.9999$ (a near-critical infall). The particle trajectories corresponding to these values of L_z are shown in Fig. 9 for $E = 3$.

Not surprisingly, ultrarelativistic infalls radiate much more energy for a given value of L_z/L_{crit} . It is also apparent from Fig. 10 that the energy output increases (and higher multipoles become relatively more important) as L_z/L_{crit} grows at fixed particle energy E . For kinetic-energy dominated infalls the energy spectrum approaches a nonzero constant as $M\omega \rightarrow 0$. The spectrum is flat for small frequencies in the head-on limit [25–28], but the slope of the spectrum for $M\omega \ll 1$ is nonzero when the infall is nonradial. In all cases the energy spectrum decays exponentially at frequencies $\omega > \omega_{\text{QNM}}^l$, where ω_{QNM}^l is the fundamental Schwarzschild QNM frequency for the given multipole [30, 31].

It is instructive to look at the multipolar structure of the radiation as we vary m for fixed l . Figure 11 shows spectra for the dominant quadrupolar component ($l = 2$) and all allowed values of m ($|m| \leq l$) for nonrelativistic infalls ($E = 1$) and kinetic energy-dominated infalls ($E = 3$) with $L_z/L_{\text{crit}} = 0, 0.9, 0.9999$. In the head-on case the $(l + m)$ -odd components vanish, and components with the same $|m|$ are exactly equal to each other because of symmetry. When $L_z \neq 0$ the particle motion breaks this degeneracy: the odd- m components are no longer zero, but they are still suppressed in the ZFL. The $l = m$ ($l = -m$) components of the spectrum emerge from the ZFL with a positive (negative) slope, respectively. For large energies this slope is independent of the particle energy and proportional to the impact parameter, in qualitative agreement with the predictions of the toy model of section III.

For intermediate frequencies, the ZFL model of section III would predict a resonance in the spectrum at the rotational frequency of the rod, and a $1/(\omega - \omega_0)$ dependence near resonance. The perturbative spectra (as

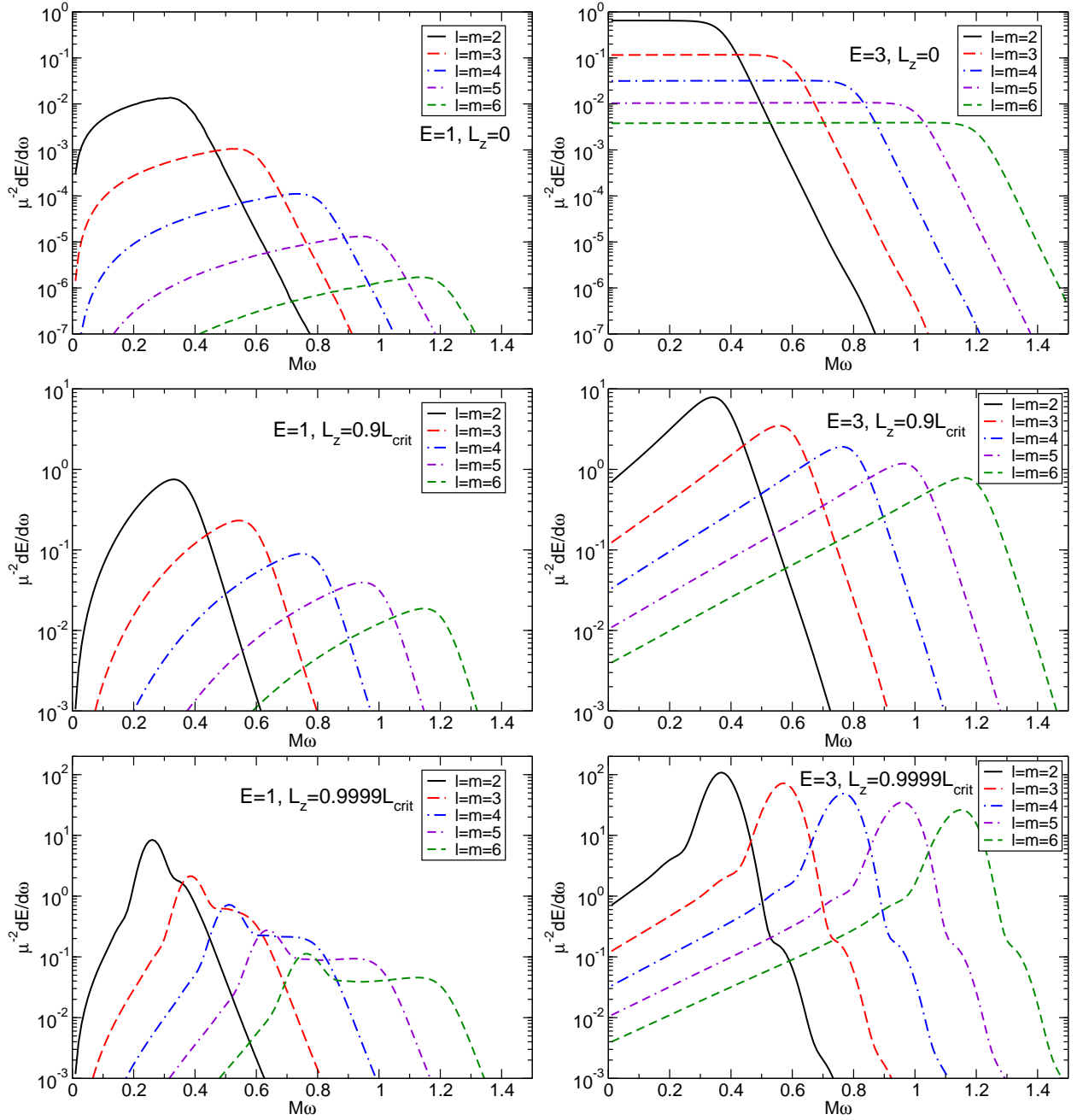


FIG. 10: Spectra for $l = m = 2, \dots, 6$ for nonrelativistic infalls ($E = 1$, left column) and kinetic energy-dominated infalls ($E = 3$, right column). The top row refers to a radial infall, the middle (bottom) row to an infall with $L/L_{\text{crit}} = 0.9$ ($L/L_{\text{crit}} = 0.9999$).

well as the NR spectra shown in section V below) are instead characterized by an exponential decay for frequencies larger than the fundamental QNM frequency of the given multipole. This difference can be attributed to the fundamentally different nature of the final state. In the toy model the final state consists of two particles attached to a massless rod, with rotation frequency determined by angular momentum conservation (and an ad-hoc functional form of the stresses). In NR simulation and point-particle infalls, the post-plunge dynamics

is dominated by the QNMs of the final BH.

The m -even components all tend to the ZFL as $M\omega \rightarrow 0$, while the m -odd components are suppressed in the same limit. The dominant ($l = m$) components of the spectra have a maximum corresponding to the QNM frequency and decay (roughly) exponentially for $\omega > \omega_{\text{QNM}}^l$. In agreement with the toy model discussed in section III, our perturbative results indicate that the ZFL of the spectra depends very weakly on the impact parameter, which (we recall again) is related to L_z by Eq. (2). This

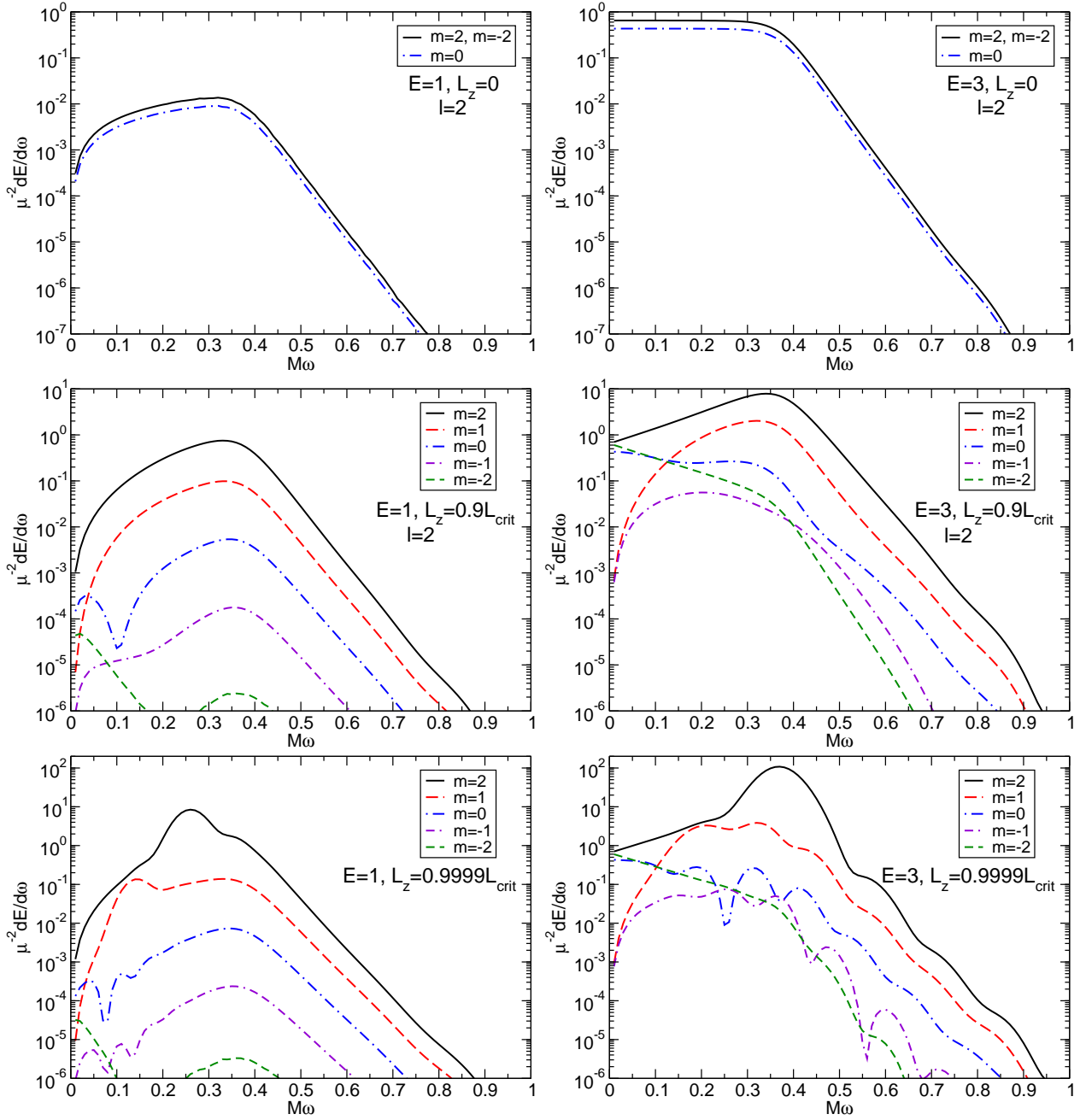


FIG. 11: Spectra for $l = 2$ and $|m| \leq l$ for nonrelativistic infalls ($E = 1$, left column) and kinetic energy-dominated infalls ($E = 3$, right column). The top row refers to a radial infall, the bottom row to an infall with $L/L_{\text{crit}} = 0.9$.

is shown very clearly in Table I.

A close inspection of the right panels of Fig. 11 shows that the ZFL of the spectrum for $m = 0$ is not the same as for $m = \pm 2$. In fact, since the ZFL is almost independent of L_z , one can use the head-on results to predict the relative ratio between modes with $m = 0$ and $|m| = 2$. In the head-on case, in a frame where the z -axis is aligned with the collision axis, only $m = 0$ modes would contribute to the radiation. Once we rotate this “natural” coordinate system to the reference frame used in this paper, where

a radial infall occurs along the x -axis (see Fig. 9), for small L_z the spectrum for (say) $m = 2$ will be related to the spectrum for $m = 0$ by [60]:

$$\lim_{\omega \rightarrow 0} \frac{dE_{22}/d\omega}{dE_{20}/d\omega} = \frac{3}{2}. \quad (61)$$

Our results for both equal-mass (see Fig. 19 below) and extreme-mass ratio head-on collisions (Fig. 11) are in very good agreement with this prediction.

TABLE I: The numerically computed ZFL of the spectrum for different values of E is compared to the analytical prediction from a multipolar decomposition of the ZFL formula (39), explained in Appendix B. The agreement is remarkable.

L_z/L_{crit}	$\frac{1}{(\mu E)^2} dE_{20}^{\text{rad}}/d\omega _{\omega=0}$			
	$E = 1.5$	$E = 3$	$E = 10$	$E = 100$
0.000	0.0160	0.0481	0.0644	0.0663
0.500	0.0160	0.0480	0.0643	0.0662
0.750	0.0159	0.0480	0.0642	0.0662
0.900	0.0159	0.0480	0.0642	0.0661
0.950	0.0159	0.0479	0.0641	0.0661
0.990	0.0159	0.0479	0.0641	0.0661
0.999	0.0159	0.0479	0.0641	0.0661
ZFL:	0.0158	0.0481	0.0644	0.0663

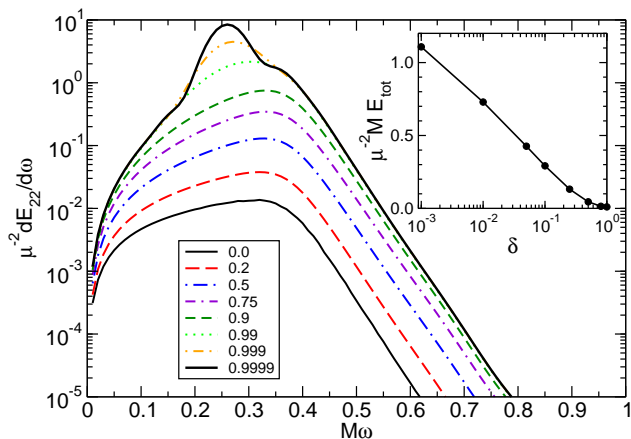


FIG. 12: Infall from rest: spectra for $l = m = 2$ as $L_z/L_{\text{crit}} \rightarrow 1$. In the inset: logarithmic divergence of the total radiated energy in the same limit.

The energy spectra with $L_z/L_{\text{crit}} = 0.9, 0.9999$ display secondary peaks which are related to the orbital motion of the particle. Radiation of orbital nature becomes more and more important as L_z grows. Indeed, the nature of the spectra changes quite significantly as $L_z/L_{\text{crit}} \rightarrow 1$. In Fig. 12 we show the $l = m = 2$ component of the spectrum for infalls from rest as we fine-tune the angular momentum to the critical value for a plunge: a very distinctive “bump” appears at a frequency which is slightly *lower* than the QNM frequency, significantly enhancing the radiated energy. The location of this “bump” corresponds to (twice) the orbital frequency of the particle at the marginally bound orbit, i.e. $\omega = 2\Omega_{\text{mb}} = (4M)^{-1}$. For infalls from rest, a particle with $L = L_{\text{crit}}$ will orbit around the marginally bound circular geodesic. The reason for this local maximum in the spectrum is that when $L_z \rightarrow L_{\text{crit}}$ the particle orbits a large number of times close to the circular marginally bound orbit at $r = 4M$.

Gravitational radiation significantly affects near-critical geodesics for purely kinematical reasons. As $L_z/L_{\text{crit}} \rightarrow 1$ the particle circles an infinite number of

times around the marginally bound circular orbit with radius $r = r_{\text{mb}}$, taking an infinite amount of proper time to reach the horizon. The proximity of the orbit to criticality is conveniently described by a small dimensionless parameter

$$\delta \equiv 1 - \frac{L_z}{L_{\text{crit}}}. \quad (62)$$

As $\delta \rightarrow 0$ the particle hovers at a circular geodesic $N \simeq -(\Omega_{\text{crit}} \dot{t}_{\text{crit}} \log(k\delta)) / (\pi\sqrt{2V_{\text{eff}}''})$ times before plunging [61]. In our case V_{eff} denotes the Schwarzschild effective radial potential, so that $r^5 V_{\text{eff}}'' = -24ML^2 + 6rL^2 - 4Mr^2$; the angular velocity $\Omega \equiv d\phi/dt$, dots stand for derivatives with respect to proper time and k is a constant. All quantities are evaluated at the critical circular geodesic with $L = L_{\text{crit}}$, and radius $r = r_{\text{crit}}$. When $E = 1$ this circular geodesic corresponds to the marginally bound orbit, located at $r_{\text{mb}} = 4M$, $M\Omega_{\text{mb}} = 8^{-1}$ and

$$N \sim -\frac{1}{\pi\sqrt{2}} \log \delta. \quad (63)$$

In the ultrarelativistic limit $E \rightarrow \infty$ the critical circular geodesic is located at the light ring $r_{\text{crit}} = 3M$, the corresponding orbital frequency $M\Omega_{\text{crit}} = (3\sqrt{3})^{-1}$ and

$$N \sim -\frac{1}{2\pi} \log(2\delta). \quad (64)$$

The orbital frequency at the light ring is intimately related with the eikonal (long-wavelength) approximation of the fundamental QNM frequency of a BH [41, 62–64]. This implies that ultrarelativistic infalls with a near-critical impact parameter are in a sense the most “natural” and efficient process to resonantly excite the dynamics of a BH. The proper oscillation modes of a Schwarzschild BH cannot be excited by particles on *stable* circular orbits (i.e. particles with orbital radii $r > 6M$ in Schwarzschild coordinates), but near-critical ultrarelativistic infalls are such that the orbital “bump” visible in Figure 12 moves just slightly to the right to overlap with the “knee” due to quasinormal ringing. So ultrarelativistic infalls have *just the right orbital frequency to excite BH oscillations*. Resonant gravitational wave scattering explains the huge increase in radiated energy that can be observed in the bottom right panels of Figs. 10 and 11 (see also [65–67]). Since QNMs are essentially perturbations of circular orbits at the light ring, we can expect that these conclusions will still apply to Kerr and even Kerr-Newman BHs [63, 64].

For near-critical orbits, the bottom panels of Fig. 11 show that the peak in the $(l = 2, m = 2)$ component is located at twice the frequency corresponding to the peak in the $(l = 2, m = 1)$ component. The source term for a particle in circular orbit with frequency Ω typically contains a term proportional to $\delta(\omega - m\Omega)$; this lends further support to the “orbital” nature of the radiation enhancement. In fact, the inset of Fig. 12 shows that the *total* radiated energy in the limit $L_z \rightarrow L_{\text{crit}}$ scales logarithmically with δ , and hence linearly with the number of orbits

N , as expected for orbital radiation in the nonresonant case. In fact, in the next subsection we will show that our numerics are in *quantitative* agreement with the energy output of a particle in circular orbit at the marginally bound geodesic.

B. Energy distribution

We now turn our attention to the total integrated energy. To simplify the discussion we start by revisiting and extending the analysis of infalls from rest ($E = 1$) first carried out by Oohara and Nakamura [51]. This reanalysis is useful both as a code check and to stress some important characteristics of the radiation in the near-critical limit $L_z/L_{\text{crit}} \rightarrow 1$. Then we generalize our findings to infalls with arbitrary energy.

1. Infall from rest ($E = 1$)

Any numerical calculation is necessarily limited to a finite number of multipoles. In this paper we computed multipolar components of the radiation up to $l = l_{\text{max}} = 6$, but to get the total radiated energy, angular momentum and linear momentum we should in principle compute the infinite sums of Eqs. (57), (58) and (59). This requires fitting the numerical results for $l \leq l_{\text{max}}$ by some analytical formula, and extrapolating this formula to estimate the contribution from multipoles with $l > l_{\text{max}}$. For infalls from rest, our results are consistent with the functional dependence proposed by Oohara and Nakamura [51]:

$$\frac{M}{\mu^2} E_l^{\text{rad}} = a_E e^{-b_E l}. \quad (65)$$

TABLE II: Fitting coefficients in Eqs. (65) and (72). For each value of L_z/L_{crit} the first line refers to a fit including all multipoles, the second line to a fit dropping the $l = 2$ multipole. A number such as 1.042(-2) means 1.042×10^{-2} .

L_z/L_{crit}	a_E	b_E	$M/\mu^2 E^{\text{rad}}$	a_J	b_J	$1/\mu^2 J^{\text{rad}}$
0.000	0.45	1.99	1.04(-2)	0.00	0.00	0.00
	0.38	1.95	1.04(-2)	0.00	0.00	0.00
0.200	0.30	1.66	1.46(-2)	1.71	1.66	8.20(-2)
	0.23	1.61	1.46(-2)	1.29	1.61	8.21(-2)
0.500	0.31	1.18	4.50(-2)	2.51	1.24	3.22(-1)
	0.24	1.13	4.50(-2)	1.75	1.16	3.23(-1)
0.750	0.47	0.92	1.32(-1)	3.60	0.96	8.98(-1)
	0.37	0.87	2.32(-1)	2.58	0.90	8.99(-1)
0.900	0.76	0.79	2.92(-1)	5.59	0.83	1.94
	0.61	0.75	2.93(-1)	4.14	0.77	1.95
0.950	1.02	0.76	4.27(-1)	7.53	0.80	2.85
	0.82	0.72	4.28(-1)	5.63	0.75	2.86
0.990	1.76	0.77	7.30(-1)	13.09	0.80	4.99
	1.36	0.72	7.32(-1)	9.68	0.74	5.01

A fit of the data yields the coefficients listed in Table II. The fitting coefficients listed in the first row are obtained by fitting all data ($2 \leq l \leq 6$). The lowest multipole $l = 2$ is usually an outlier in this fit. As a rough check of the accuracy of the extrapolation, we repeat the fit considering only numerical data with $3 \leq l \leq 6$; this yields the coefficients listed in the second row. The difference between the total energies obtained by these two procedures can be seen as a very rough estimate of the error involved in the extrapolation. It is quite clear from the table that this error increases as $L_z/L_{\text{crit}} \rightarrow 1$. This is of course a lower limit on the overall error in the computed energy, because it does not take into account numerical errors in the data, systematic errors coming from the (somewhat arbitrary) choice of the fitting function, and inaccuracies in the fit itself. In any event, our fits are in good (but not perfect) agreement with the entries in Table I of Oohara and Nakamura [51]. Oohara and Nakamura do not specify the range in l used for their fits, so it is hard to say if the slight difference in fitting coefficients is due to small differences in the numerics or to the fitting procedure itself.

A fit to our perturbative results close to the critical angular momentum for capture yields

$$\frac{M}{\mu^2} E^{\text{rad}} = -0.0375 - 0.172 \log \delta. \quad (66)$$

where δ was defined in Eq. (62).

The analysis of the previous section reveals that close to the critical value of the angular momentum (i.e. as $\delta \rightarrow 0$) the total radiated energy E^{rad} should scale as

$$\frac{M}{\mu^2} E^{\text{rad}} \simeq k + E_{N=1} N, \quad (67)$$

where $E_{N=1}$ is the energy radiated in one revolution close to the circular marginally bound geodesic, and k is an undetermined constant. Early calculations by Deweiler [49, 50] (that we confirmed using a FORTRAN code discussed, for example, in Ref. [68]) show that $\frac{M}{\mu^2} E_{N=1} \simeq 0.65$ for circular orbits with $r_{\text{crit}} = 4M$ in Schwarzschild. Using Eq. (63) one gets the independent estimate

$$\frac{M}{\mu^2} E^{\text{rad}} \simeq k - 0.15 \log \delta, \quad (68)$$

which is in good agreement with the fit of Eq. (66).

2. Ultrarelativistic infall

For ultrarelativistic collisions the scaling with l is not exponential, as illustrated in Fig. 13. In fact, we find that a power law of the form

$$\frac{M E_l^{\text{rad}}}{(\mu E)^2} = c_E l^{-d_E}, \quad (69)$$

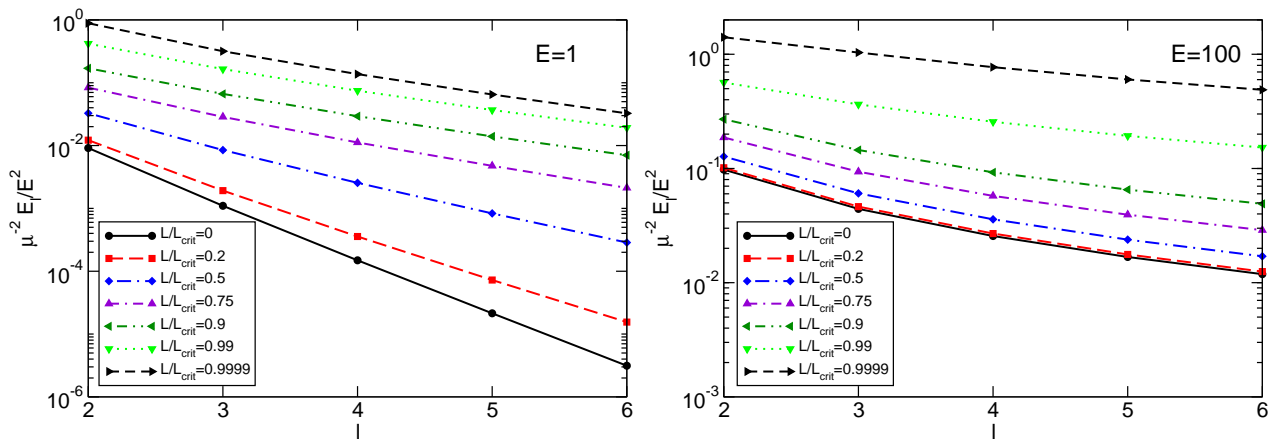


FIG. 13: Multipolar energy distribution for E_l/E^2 for $E = 1$ (left) and $E = 100$ (right). For large E the radiated energy scales like E^2 , not like μ^2 . Higher multipoles contribute (relatively) more when E is large. The scaling with l is well approximated by an exponential for collisions from rest and by a power law for relativistic collisions.

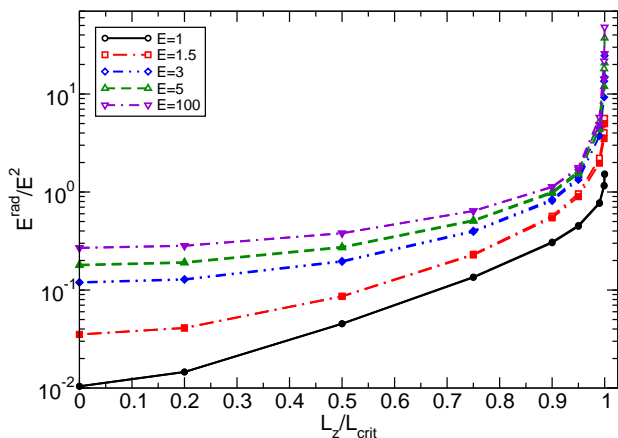


FIG. 14: Total energy radiated $M/(\mu E)^2 E^{\text{rad}}$ rescaled by the particle energy squared, as a function of L_z/L_{crit} . In extrapolating for $l > 6$, the fitting coefficients in Eqs. (65) and (69) were obtained either including (empty symbols) or excluding (filled symbols) the $l = 2$ data. The difference is only visible in the limit $L_z/L_{\text{crit}} \rightarrow 1$.

describes well our numerical results, where c_E and d_E are constants. A least-squares fit yields the values of c_E , d_E and the total radiated energy E^{rad} listed in Table III.

For $L_z = 0$ and large E we get $E^{\text{rad}}/(\mu E)^2 = 0.26$, in agreement with the results of Refs. [25, 28]. Close to the critical angular momentum ($L_z \rightarrow L_{\text{crit}}$) the fit yields $E_l \sim 1/l$. As explained in section IV B, in the limit $E \rightarrow \infty$ the radiation is dominated by energy emitted at the light ring (the marginally bound circular geodesic located at $r = 3M$). Our fit is perfectly consistent with the classic study of synchrotron radiation by Davis *et al.* [48], who found precisely a $1/l$ dependence for the multipolar dependence of the radiation emitted by a particle orbiting at the circular null geodesic.

For $L_z/L_{\text{crit}} < 0.95$ we get the following fits for the total radiated energy as a function of the angular momentum (see Fig. 14):

$$\begin{aligned} \frac{ME^{\text{rad}}}{(\mu E)^2} &= 0.0685 \exp \left[3.241 \left(\frac{L_z}{L_{\text{crit}}} \right)^4 \right], (E = 1.5), \\ \frac{ME^{\text{rad}}}{(\mu E)^2} &= 0.145 \exp \left[2.778 \left(\frac{L_z}{L_{\text{crit}}} \right)^4 \right], (E = 3), \\ \frac{ME^{\text{rad}}}{(\mu E)^2} &= 0.294 \exp \left[2.176 \left(\frac{L_z}{L_{\text{crit}}} \right)^4 \right], (E = 100). \end{aligned} \quad (70)$$

These results should be compared with the fit of the energy computed from NR simulations of equal-mass BHs [6]:

$$\frac{E^{\text{rad}}}{M_{\text{ADM}}^2} = 0.0195 \exp \left[2.632 \left(\frac{L_z}{L_{\text{crit}}} \right)^4 \right], (E = 1.5). \quad (71)$$

In the fit to NR results (which have a numerical error of about 5%) the radiated energy is normalized to M_{ADM} and we estimate L_z/L_{crit} to be given by b/b_{crit} [6]. Unfortunately, close to L_{crit} it is extremely difficult to get accurate estimates for E^{rad} , because higher multipoles make an important contribution to the total radiation.

C. Angular momentum

1. Infall from rest ($E = 1$)

Let us consider the angular momentum carried by the radiation. For slow motion, the multipolar decomposition of the radiated angular momentum is consistent with

TABLE III: Fitting coefficients in Eq. (69). For each value of L_z/L_{crit} the first line refers to a fit keeping all multipoles, the second line to a fit dropping the $l = 2$ multipole.

L_z/L_{crit}	$E = 1.5$			$E = 3$			$E = 10$			$E = 100$		
	c_E	d_E	$\frac{M}{(\mu E)^2} E^{\text{rad}}$	c_E	d_E	$\frac{M}{(\mu E)^2} E^{\text{rad}}$	c_E	d_E	$\frac{M}{(\mu E)^2} E^{\text{rad}}$	c_E	d_E	$\frac{M}{(\mu E)^2} E^{\text{rad}}$
0.000	1.75	5.51	0.035	6.80(-1)	3.10	0.12	3.99(-1)	2.06	0.24	3.67(-1)	1.92	0.27
	6.82	6.39	0.035	1.11	3.41	0.12	4.16(-1)	2.08	0.24	3.56(-1)	1.90	0.27
0.200	1.26	4.96	0.041	6.71(-1)	3.01	0.13	4.09(-1)	2.04	0.25	3.78(-1)	1.90	0.28
	3.74	5.66	0.041	1.06	3.31	0.13	4.28(-1)	2.07	0.25	3.69(-1)	1.89	0.28
0.500	7.24(-1)	3.50	0.086	6.61(-1)	2.60	0.20	4.86(-1)	1.93	0.35	4.52(-1)	1.83	0.38
	1.26	3.86	0.086	9.08(-1)	2.81	0.19	5.11(-1)	1.97	0.34	4.53(-1)	1.83	0.38
0.750	7.38(-1)	2.56	0.23	7.50(-1)	2.13	0.40	6.55(-1)	1.77	0.61	6.06(-1)	1.70	0.64
	1.01	2.76	0.23	8.90(-1)	2.24	0.39	6.82(-1)	1.79	0.60	6.06(-1)	1.70	0.64
0.900	0.91	2.02	0.57	8.86(-1)	1.76	0.84	8.42(-1)	1.58	1.14	7.95(-1)	1.55	1.13
	1.16	2.17	0.54	9.94(-1)	1.83	0.81	8.85(-1)	1.61	1.11	8.08(-1)	1.56	1.12
0.950	1.10	1.80	0.96	1.00	1.56	1.41	9.75(-1)	1.45	1.80	9.33(-1)	1.43	1.77
	1.41	1.96	0.90	1.12	1.63	1.33	1.04	1.49	1.71	9.75(-1)	1.46	1.71
0.990	1.81	1.62	2.22	1.41	1.27	4.48	1.36	1.20	5.76	1.32	1.20	5.77
	2.42	1.81	1.97	1.62	1.36	3.74	1.51	1.27	4.78	1.45	1.26	4.86

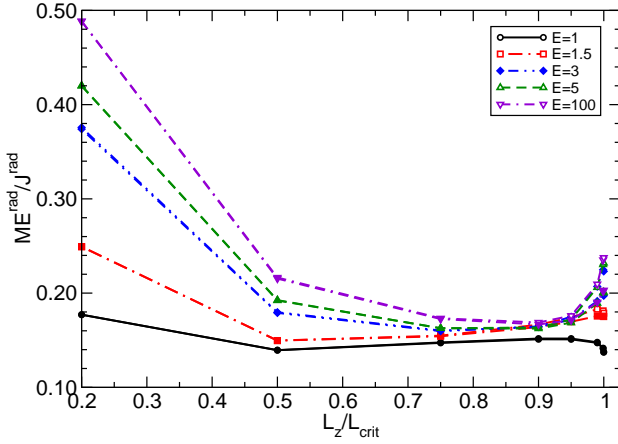


FIG. 15: Ratio $ME^{\text{rad}}/J^{\text{rad}}$ for different values of E . The meaning of filled and empty symbols is the same as in Fig. 14. Oohara and Nakamura [51] find that this ratio is $\simeq 0.15 \pm 0.01$ for $1 \lesssim L_z \lesssim 3.9$ when $E = 1$ and $L_{\text{crit}} = 4$, but we expect that $E^{\text{rad}}/J^{\text{rad}} \simeq (M\Omega_{\text{scat}})$ as $L_z/L_{\text{crit}} \rightarrow 1$ (see text).

the exponential dependence

$$\frac{1}{\mu^2} J_l^{\text{rad}} = a_J e^{-b_J l}, \quad (72)$$

where the coefficients a_J , b_J are given in Table II.

As shown in Fig. 15, our results for infalls from rest are consistent with Oohara and Nakamura's [51] suggestion that for $0.25 \lesssim L_z/L_{\text{crit}} \lesssim 0.99$ the radiated angular momentum should obey the approximate relation

$$\frac{ME^{\text{rad}}}{J^{\text{rad}}} \approx (0.15 \pm 0.01). \quad (73)$$

However, this approximate proportionality relation must break down as $L_z \rightarrow L_{\text{crit}}$, because for a particle in circular motion $E^{\text{rad}}/J^{\text{rad}} \simeq (M\Omega_{\text{scat}})$ [49, 69]. For example,

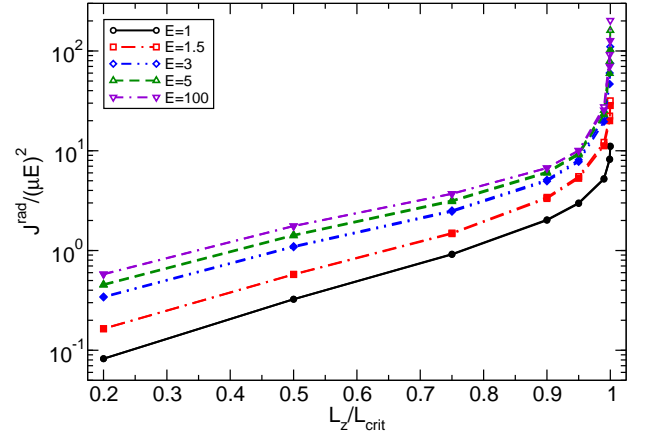


FIG. 16: Total radiated angular momentum (obtained by extrapolation) as a function of L_z/L_{crit} . The meaning of filled and empty symbols is the same as in Fig. 14.

for $E = 1$ we should find that $E^{\text{rad}}/J^{\text{rad}} \rightarrow 1/8 = 0.125$, and as $E \rightarrow \infty$ we expect that $E^{\text{rad}}/J^{\text{rad}} \rightarrow 1/(3\sqrt{3}) \simeq 0.19245$. Quite remarkably, and despite the sizeable uncertainties in extrapolating our numerical results to get the total radiated energy and angular momentum, Fig. 15 is consistent with these predictions.

2. Ultrarelativistic infall

The total radiated angular momentum for generic infall energies and its multipolar decomposition are shown in Figs. 16-17. For collisions with generic impact parameter, we find that the angular momentum emitted in a given

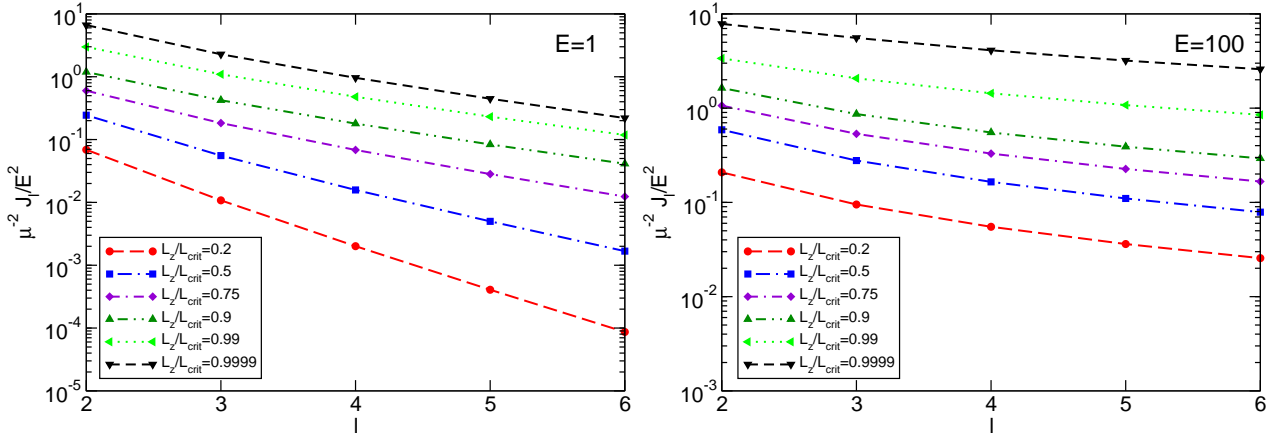


FIG. 17: Multipolar components of the radiated angular momentum J_l/E^2 for $E = 1$ (left) and $E = 100$ (right). For large E the radiated angular momentum scales like $(\mu E)^2$. Higher multipoles contribute (relatively) more when E is large. The scaling with l is logarithmic for collisions from rest, but it acquires corrections for relativistic collisions. By symmetry, no angular momentum is radiated when $L_z = 0$.

multipole l has a power-law dependence of the form

$$\frac{J_l^{\text{rad}}}{(\mu E)^2} = c_J l^{-d_J}, \quad (74)$$

where c_J and d_J are constants. The values of c_J , d_J and of the total radiated angular momentum J^{rad} obtained by extrapolation are listed in Table IV. The angular momentum emitted in each multipole $l \leq l_{\text{max}}$ is shown in Fig. 17. Using Eq. (74) we can extrapolate to get the total radiated angular momentum. Fig. 15 shows that the ratio $J^{\text{rad}}/(ME^{\text{rad}})$ for kinetic-energy dominated infalls is only (roughly) constant in the intermediate regime $0.5 \lesssim L_z/L_{\text{crit}} \lesssim 0.95$. The following expressions provide good fits to the extrapolated values:

$$\begin{aligned} \frac{J^{\text{rad}}}{(\mu E)^2} &= 0.0142 \left[1 - \exp\left(-3.170 \frac{L_z}{L_{\text{crit}}}\right) \right]^2, \quad (E = 1.5), \\ \frac{J^{\text{rad}}}{(\mu E)^2} &= 0.0676 \left[1 - \exp\left(-2.585 \frac{L_z}{L_{\text{crit}}}\right) \right]^2, \quad (E = 3), \\ \frac{J^{\text{rad}}}{(\mu E)^2} &= 0.42 \left[1 - \exp\left(-1.836 \frac{L_z}{L_{\text{crit}}}\right) \right]^2, \quad (E = 100). \end{aligned} \quad (75)$$

These fits can be compared with the corresponding fit from NR simulations of equal-mass BHs [6], which yields (within a numerical error of about 5%)

$$\frac{J^{\text{rad}}}{M_{\text{ADM}}^2} = 0.0024 \left[1 - \exp\left(-2.928 \frac{L_z}{L_{\text{crit}}}\right) \right]^2, \quad (E = 1.5). \quad (76)$$

D. Linear momentum

Representative spectra of the radiated linear momentum are shown in Fig. 18. To illustrate how different

multipoles contribute in building up the total linear momentum, and also to “visually” test the convergence of the sum in Eq. (59), we plot in different linestyles the spectra obtained by summing over the lowest l_{max} multipoles with $l_{\text{max}} = 2, \dots, 6$. Strictly speaking, if we sum Eq. (59) up to $l_{\text{max}} = 6$ the last term of the sum will be inconsistent, because it involves amplitudes such as $X_{l+1, m+1}$, which we have not computed and we set to zero for lack of a better alternative. Note that this “multipolar coupling” does not occur in the calculation of the energy and angular momentum. The inconsistent truncation means that we should only consider these plots as representative of the real convergence properties of the sum for $l_{\text{max}} \leq 5$. Furthermore, the spectrum obtained when we truncate at $l_{\text{max}} = 6$ cannot be trusted in fitting numerical results to extrapolate the sum to infinity. For this reason (and also for the highly oscillatory buildup of linear momentum which is evident from Fig. 18) the extrapolation of numerical results to get the total radiated linear momentum is quite sensitive to the relatively low number of multipoles that we are using.

1. Infall from rest ($E = 1$)

Despite these caveats, in the case of low-energy collisions (and in particular for infalls from rest) the total linear momentum converges reasonably fast with l . Summing over $2 \leq l \leq 6$ is typically enough to warrant an accuracy of 10% or less in the total linear momentum.

Nevertheless we have used extrapolation, fitting our numerical results by an exponential:

$$P_{l_{\text{max}}} = P^{\text{rad}} - a_P e^{-b_P l_{\text{max}}}, \quad (77)$$

The fitting coefficients and the total radiated momentum obtained by extrapolation are listed in Table V.

TABLE IV: Fitting coefficients in Eq. (74). For each value of L_z/L_{crit} the first line refers to a fit keeping all multipoles, the second line to a fit dropping the $l = 2$ multipole.

L_z/L_{crit}	$E = 1.5$			$E = 3$			$E = 10$			$E = 100$		
	c_J	d_J	$1/(\mu E)^2 J^{\text{rad}}$	c_J	d_J	$1/(\mu E)^2 J^{\text{rad}}$	c_J	d_J	$1/(\mu E)^2 J^{\text{rad}}$	c_J	d_J	$1/(\mu E)^2 J^{\text{rad}}$
0.000	0.00	0.00	0.00	0.00	0.00	0.00	0.00	0.00	0.00	0.00	0.00	0.00
	0.00	0.00	0.00	0.00	0.00	0.00	0.00	0.00	0.00	0.00	0.00	0.00
0.200	3.79	4.60	0.16	1.30	2.71	0.35	0.82	1.98	0.54	0.78	1.91	0.58
	11.49	5.32	0.16	1.89	2.95	0.34	0.83	1.99	0.54	0.76	1.89	0.58
0.500	5.22	3.58	0.58	3.11	2.45	1.10	2.20	1.89	1.68	2.09	1.83	1.75
	9.62	3.98	0.57	4.15	2.64	1.08	2.24	1.90	1.67	2.05	1.82	1.76
0.750	5.55	2.70	1.50	4.48	2.09	2.52	3.62	1.72	3.65	3.42	1.69	3.69
	7.60	2.90	1.47	5.40	2.21	2.45	3.72	1.74	3.61	3.38	1.68	3.71
0.900	6.59	2.15	3.41	5.76	1.79	5.11	5.11	1.58	6.88	4.84	1.56	6.70
	8.09	2.28	3.32	6.46	1.87	4.94	5.25	1.60	6.77	4.82	1.56	6.72
0.950	7.77	1.93	5.51	6.65	1.63	8.09	6.11	1.48	10.40	5.83	1.47	10.08
	9.43	2.06	5.29	7.30	1.69	7.75	6.33	1.50	10.13	5.89	1.48	9.98
0.990	11.85	1.71	12.15	9.02	1.35	21.65	8.45	1.26	27.81	8.14	1.26	27.54
	15.02	1.86	11.22	9.96	1.42	19.52	8.98	1.30	25.35	8.53	1.29	25.55

TABLE V: Fitting coefficients in Eq. (77). The first line refers to a fit including all multipoles, the second line to a fit dropping $l = 2$.

L_z/L_{crit}	a_P	b_P	$M/\mu^2 P^{\text{rad}}$
0.000	7.03(-3)	2.00	8.33(-4)
	7.98(-3)	2.05	8.33(-4)
0.200	1.09(-2)	1.56	2.41(-3)
	9.99(-3)	1.53	2.42(-3)
0.500	3.05(-2)	1.13	1.16(-2)
	2.58(-2)	1.06	1.16(-2)
0.750	6.54(-2)	0.84	3.37(-2)
	5.55(-2)	0.78	3.39(-2)
0.900	9.24(-2)	0.67	5.75(-2)
	8.13(-2)	0.61	5.81(-2)
0.950	8.85(-2)	0.58	6.20(-2)
	7.83(-2)	0.52	6.30(-2)
0.990	6.77(-2)	0.72	4.96(-2)
	4.03(-2)	0.48	5.16(-2)

2. Ultrarelativistic infall

Spectra of the linear momentum radiated by ultrarelativistic infalls are shown in Fig. 18. For head-on collisions, in the limit of large boosts the radiated momentum is well described by

$$P^{\text{rad}} = \left(0.11 - \frac{0.33}{E^{1.37}} \right) \frac{(\mu E)^2}{M}, \quad E \rightarrow \infty. \quad (78)$$

For ultrarelativistic infalls the ZFL of the spectrum is nonvanishing and it depends very weakly on the impact parameter (we observed a similar trend when studying the ZFL of the spectrum of the radiated energy). The ZFL is very well approximated by Smarr's formula, Eq. (47). This is shown quantitatively in Table VI.

TABLE VI: The ZFL of the radiated linear momentum for head-on collisions, compared with the analytical result (47).

L_z/L_{crit}	$\frac{1}{(\mu E)^2} dP^{\text{rad}}/d\omega _{\omega=0}$				
	$E = 1.5$	$E = 3$	$E = 5$	$E = 10$	$E = 100$
0.00	0.0182	0.100	0.151	0.187	0.203
ZFL:	0.0180	0.0993	0.150	0.189	0.212

We tried to fit our numerical results for high energy and generic impact parameters by a power law of the form $P_{\text{max}} = P^{\text{rad}} - c_P l_{\text{max}}^{-d_P}$. For the reasons explained above, the errors associated with this extrapolation procedure are significant, and we decided not to present the extrapolated values of P^{rad} .

Qualitatively, in the ultrarelativistic case the total radiated linear momentum increases only mildly with the impact parameter: we find a maximum increase of a factor ~ 3 relatively to the head-on case. This observation can be used to give a rough estimate of the maximum recoil that could result from gravitational-wave emission in the ultrarelativistic collision of nonspinning BHs. If we take $\mu E/M = 1/10$ we get a recoil velocity of order $v \sim 10^{-3}$ for head-on collisions, and a maximum of around $v \sim 3 \times 10^{-3}$ for grazing collisions. Restoring physical units, this would correspond to recoils in the range 300 – 900 km/s. It will be interesting to verify these estimates by NR simulations of ultrarelativistic, comparable-mass BH binaries.

V. COMPARING DIFFERENT APPROACHES

As discussed in Ref. [4] (see also Fig. 1), NR results for the energy spectra from the high-energy, head-on collision of two BHs are in very good agreement with

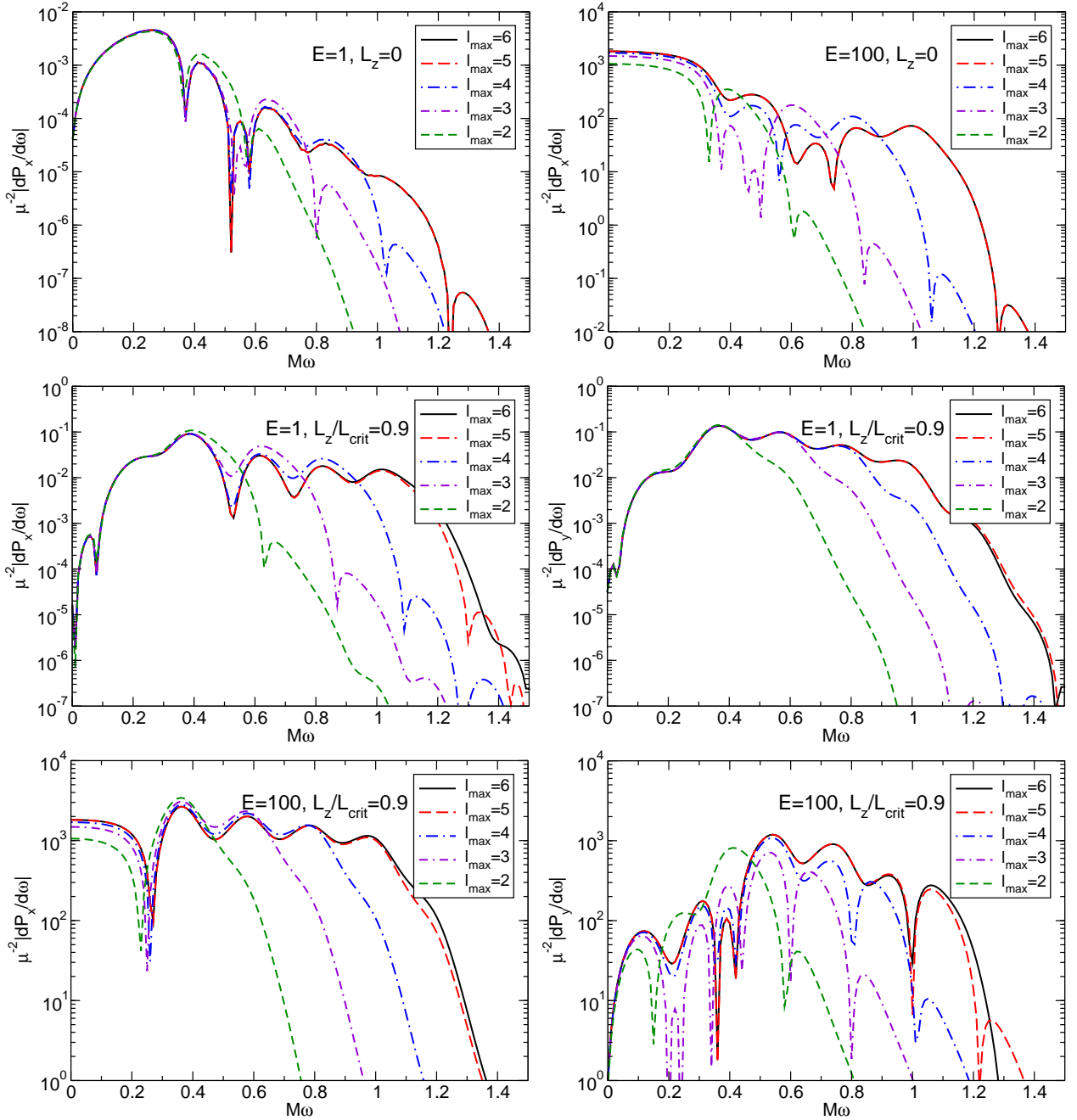


FIG. 18: Spectra of the linear momentum radiated for infalls from rest ($E = 1$) and ultrarelativistic infalls ($E = 100$). Different lines refer to different truncation choices in the sum of Eq. (59). In the head-on case (top row) the only nonzero component of the linear momentum is P_x ; for $L_z/L_{\text{crit}} = 0.9$ (middle and bottom rows) both the P_x and P_y components are nonzero. To test convergence we sum Eq. (59) up to different values of l_{max} , as indicated in the legend.

the ZFL predictions. Calculations of the radiation from point particles falling into nonrotating BHs are in quantitative agreement with ZFL predictions in the extreme-mass ratio limit (see for instance Table I), and in qualitative agreement with NR calculations. In this section we present a more extensive comparison between these different approaches.

A. Head-on collisions

For head-on collisions, the ZFL results of section III are in qualitative and quantitative agreement with point-particle calculations. In particular, a multipolar decomposition of ZFL calculations yields a flat energy spectrum for all multipolar components (see Appendix B). Point-

particle calculations and NR simulations suggest that the cutoff frequency for each multipole can be chosen to be the lowest QNM frequency for the given multipole. A multipolar analysis is therefore important to introduce a more “natural” and appealing cutoff frequency in the ZFL spectrum, in contrast with Smarr’s original, qualitative suggestions [20].

In the eikonal limit, the real part of the fundamental QNM frequency for the l -th multipole ω_{QNM}^l is related to the frequency $M\Omega_c = (3\sqrt{3})^{-1}$ of unstable circular null geodesics [31, 41]:

$$\omega_{\text{QNM}}^l = l\Omega_c, \quad (79)$$

Combining this approximation (which is surprisingly good even for low values of l) with ZFL calculations of the energy spectrum at low frequencies, we can estimate the total radiated energy as follows:

$$E^{\text{rad}} \sim \sum_{l=2}^{\infty} \left. \frac{dE_l}{d\omega} \right|_{\omega=0} \times \omega_{\text{QNM}}^l. \quad (80)$$

At high energies the ZFL assumes a particularly simple form. Using the multipolar decomposition results from Appendix B we get, for the equal-mass case:

$$\begin{aligned} E^{\text{rad}} &\simeq \sum_{\text{even } l} \frac{4(EM)^2 (2l+1)(l-2)!}{\pi (l+2)!} l\Omega_c \\ &= \frac{4 \log 2}{3\sqrt{3}\pi} EM \simeq 0.1698 EM. \end{aligned} \quad (81)$$

Here we used $EM\Omega_c = (3\sqrt{3})^{-1}$, since the final BH has (approximately) mass EM . An extrapolation of results from recent NR simulations [4] predicts $E^{\text{rad}} \simeq (0.14 \pm 0.03)M_{\text{ADM}}$, in remarkably good agreement with this naive estimate.

As another example, let us consider the extreme mass-ratio case in the high-energy limit. Using again results from Appendix B we get

$$\begin{aligned} E^{\text{rad}} &\simeq \sum_l \frac{4E^2\mu^2 (2l+1)(l-2)!}{\pi (l+2)!} l\Omega_c \\ &= \frac{13}{9\sqrt{3}\pi} \frac{\mu^2 E^2}{M} \simeq 0.265 \frac{\mu^2 E^2}{M}. \end{aligned} \quad (82)$$

The extrapolation of point-particle results to $E \rightarrow \infty$ (see [25, 28] and Table III) predicts $E^{\text{rad}} \sim 0.262\mu^2 E^2/M$ [25], again in remarkable agreement with our simple approximation.

B. Collisions with finite impact parameter

Unfortunately, an extension of our head-on estimates to the generic case of collisions with finite impact parameter is not straightforward, because the energy spectrum is no longer flat. However several generic features are common to the ZFL, point-particle and full NR calculations.

Fig. 19 illustrates our point. In the left panel we show the energy spectra (rescaled by the total ADM mass) for NR simulations of equal-mass BH collisions with $E = 1.5$ and varying impact parameter b . In the right panel we show spectra for point particles falling into a Schwarzschild BH of mass M with energy $E = 1.5$ and different impact parameters. The angular momentum of the particle normalized by the critical angular momentum (which for $E = 1.5$ is $L_{\text{crit}} \simeq 6.35M$) is indicated in the legend. Strictly speaking, these two plots can only be compared from a qualitative point of view. In the equal-mass case the final BH is spinning (in fact, for large impact parameters it is rapidly spinning [6]), whereas our point-particle calculation considers nonspinning holes. Nevertheless, the spectra show qualitative agreement. In particular, the ZFL is independent of the impact parameter for both equal-mass and extreme-mass ratio collisions. For point particles falling into Schwarzschild BHs the cutoff frequency does not depend on m , but early calculations of nonrelativistic equatorial infalls into Kerr BHs [55–57] hint that this degeneracy in the cutoff frequency should be lifted when one considers the rotating case.

For small, but finite frequencies, we find that the spectrum of positive- m (negative- m) modes has positive (negative) slope as $\omega \rightarrow 0$. The ZFL-inspired calculation for generic impact parameter of section III taught us that while the ZFL itself is a robust feature, the finite-frequency behavior is not, and it strongly depends on the modeling of constraining forces. Such arbitrariness is absent in the point-particle calculation.

A fit to NR results for $E = 1.5$ and $l = m = 2$ yields

$$\frac{1}{M^2} \frac{dE}{d\omega} = \left. \frac{1}{M^2} \frac{dE}{d\omega} \right|_{\omega=0} + 0.15 \frac{L_z}{L_{\text{crit}}} M\omega. \quad (83)$$

In the point-particle limit, a fit of the $l = m = 2$ spectra with $E = 1.5$ yields

$$\frac{1}{(\mu E)^2} \frac{dE}{d\omega} = \left. \frac{1}{(\mu E)^2} \frac{dE}{d\omega} \right|_{\omega=0} + 0.65 \frac{L_z}{L_{\text{crit}}} M\omega. \quad (84)$$

VI. OUTLOOK

In this paper we have used a combination of ZFL calculations and perturbative techniques to study some of the main features emerging from ongoing NR simulations of ultrarelativistic BH collisions. Here we wish to point out possible extensions of our analysis.

We are currently working on a perturbative analysis of ultrarelativistic infalls with generic impact parameter into Kerr BHs (see [55–57] for studies of infalls from rest). Another obvious generalization would be to extend ZFL and point-particle calculations to higher-dimensional spacetimes. A preliminary investigation of head-on, ultrarelativistic infalls into D -dimensional (Schwarzschild-Tangherlini) BHs can be found in Ref. [28]. It would be interesting to extend that study to plunges with generic energy and impact parameter, and eventually also to rotating (Myers-Perry) BHs.

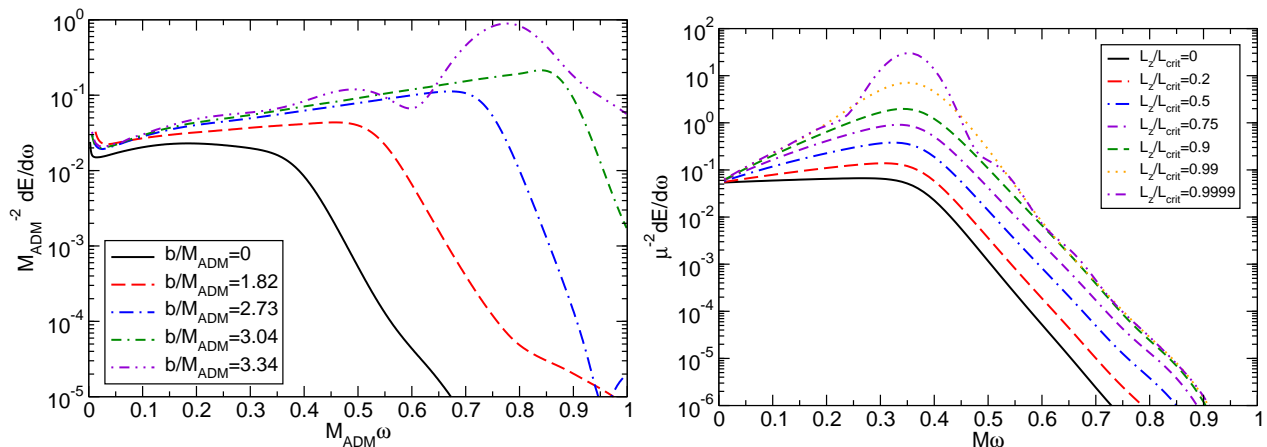


FIG. 19: Left: $l = m = 2$ component of the energy spectrum of the gravitational radiation emitted in the collision of two equal-mass BHs having speed $\beta = v/c \simeq 0.75$ in the center-of-mass frame [4, 6]. All quantities are normalized to the ADM mass of the system M_{ADM} . Right: $l = m = 2$ component of the energy spectrum of the gravitational radiation emitted by point particles falling into Schwarzschild BHs of mass M with energy $E = 1.5$.

As mentioned in the introduction, NR simulations have provided evidence of the existence of two critical thresholds, depending on the impact parameter b of the collision: for $b < b^*$ (where b^* is the *threshold of immediate merger*) the BHs merge within the first encounter; for $b^* < b < b_{\text{scat}}$ (where b_{scat} is the *scattering threshold*) the binary does not merge immediately, but sufficient energy is radiated to put the binary into a bound state that *eventually* results in a merger; finally, for $b > b_{\text{scat}}$ the BHs scatter producing bremsstrahlung radiation [6]. The emergence of these two different thresholds b_* and b_{scat} can be explained in terms of a gravitational radiation-induced splitting of the scattering threshold. This splitting can be described in terms of the so-called Melnikov function, which is well-known from the theory of dynamical systems [70]. A detailed analysis of this problem will be the topic of a future publication.

In this paper we have not discussed the radiation emitted by ultrarelativistic encounters leading to scattering, rather than BH formation. Studies of gravitational bremsstrahlung started in the sixties with the work by Peters [71], and they employed several approximation schemes. Turner and Will studied the gravitational radiation emitted as a result of the scattering in a low-velocity (post-Newtonian) approximation [72–74]. D’Eath and collaborators developed an elegant approximation to estimate the radiation in the ultrarelativistic case [75–80]. Matzner and Nutku developed a “method of virtual quanta” analogous to the Weizsäcker-Williams method of virtual quanta in electromagnetism, which is restricted to high-velocity, extreme-mass ratio encounters [81]. The most complete study of bremsstrahlung is perhaps a series of papers by Kovacs, Thorne and Crowley, who computed the radiation from compact objects of arbitrary mass ratio flying past each other at arbitrary velocities in the limit of large impact parameter [82–85].

We refer the reader to section VI of Ref. [85] for a comprehensive review of methods of computing gravitational bremsstrahlung radiation.

In the eighties, various groups worked out the gravitational radiation from particles scattering around BHs at nonrelativistic and relativistic velocities [53, 54] (see also [45] for a review). It would be interesting to repeat their perturbative calculations paying special attention to ultrarelativistic scattering and to the near-critical behavior. Moreover, a comparison of bremsstrahlung radiation as computed in NR against all these different approximations would be a very interesting topic for future work.

Yet another semianalytical approach that we have not considered in this paper, but that could certainly prove useful as a diagnostic of NR codes in D dimensions, is the close-limit approximation (see e.g. [86]). A detailed quantitative understanding of gravitational radiation from D -dimensional BH collisions will ultimately rely on the development of NR in higher dimensional spacetimes. Various groups are making rapid progress in this direction [8–11].

Acknowledgments

This work was supported by NSF grants PHY-0745779, PHY-0601459, PHY-0652995, PHY-090003, PHY-0900735, by the Alfred P. Sloan Foundation and by the Sherman Fairchild foundation to Caltech. It was partially funded by FCT - Portugal through projects PTDC/FIS/64175/2006, PTDC/FIS/098025/2008, PTDC/FIS/098032/2008, PTDC/CTE-AST/098034/2008 and CERN/FP/109290/2009. V.C. is supported by a “Ciência 2007” research contract and by Fundação Calouste Gulbenkian through a short-term scholarship. Computations were performed at TeraGrid

in Texas, Magerit in Madrid, the Woodhen cluster at Princeton University and HLRB2 Garching. The authors thankfully acknowledge the computer resources, technical expertise and assistance provided by the Barcelona Supercomputing Center - Centro Nacional de Supercomputación.

Appendix A: The Sasaki-Nakamura formalism

The gravitational radiation generated by point particles in BH backgrounds is best described in the Sasaki-Nakamura formalism [87–89]. Here we summarize the equations describing the general infall of particles of rest mass μ with arbitrary energy (per unit rest mass) E . We consider the metric of a nonrotating BH in Schwarzschild coordinates:

$$ds^2 = -f(r)dt^2 + f(r)^{-1}dr^2 + r^2 (d\theta^2 + \sin^2\theta d\phi^2), \quad (\text{A1})$$

where $f(r) \equiv 1 - 2M/r$ and M is the BH mass. In the Teukolsky formalism the perturbation equations can be reduced to a second-order differential equation for the Newman-Penrose scalar ψ_4 with a source term T_T . We can expand ψ_4 as

$$\psi_4(t, r, \Omega) = r^{-4} \int_{-\infty}^{\infty} d\omega \sum_{lm} R_{lm}(r) {}_{-2}Y_{lm}(\Omega) e^{-i\omega t}, \quad (\text{A2})$$

and similarly for T_T . We denote by ${}_sY_{lm}(\theta)$ the spin- s weighted spherical harmonic, which can be expressed in terms of the well-known (scalar) spherical harmonics [90].

For a point particle falling into a BH along a geodesic the coordinates can be parametrized in terms of (say) the radial location of the particle: $(t, r, \Omega) = (T(R), R, \Omega(R))$. The source term in Teukolsky's equation is directly related to the energy-momentum tensor $T^{\mu\nu}$ of the test particle of mass μ :

$$T^{\mu\nu} = \frac{\mu}{r^2|\dot{r}|} \delta(t - T(R)) \delta^2(\Omega - \Omega(R)) \frac{dx^\mu}{d\tau} \frac{dx^\nu}{d\tau}, \quad (\text{A3})$$

where an overdot denotes $d/d\tau$. In particular,

$$T_T \equiv 4 \int d\Omega dt \rho^{-6} \left(B'_{2\ lm} + B_{2\ lm}^* \right) e^{-im\phi} {}_{-2}Y_{lm}(\theta) e^{i\omega t}, \quad (\text{A4})$$

with

$$B'_{2\ lm} = -\frac{1}{2}\rho^9 \mathcal{L}_{-1}[\rho^{-4} \mathcal{L}_0(\rho^{-3} T_{nn})] + \frac{1}{2\sqrt{2}}\rho^9 \Delta^2 \mathcal{L}_{-1}[\rho^{-2} J_+(\Delta^{-1} \rho^{-4} T_{n\bar{m}})], \quad (\text{A5})$$

$$B_{2\ lm}^* = -\frac{1}{4}\rho^9 \Delta^2 J_+[\rho^{-4} J_+(\rho^{-1} T_{\bar{m}\bar{m}})] + \frac{1}{2\sqrt{2}}\rho^9 \Delta^2 J_+[\rho^{-2} \mathcal{L}_{-1}(\Delta^{-1} \rho^{-4} T_{n\bar{m}})]. \quad (\text{A6})$$

Here and below we generally omit the subscripts (l, m) to simplify the notation. We also define $\Delta \equiv r^2 f(r) = r^2 - 2Mr$, $\rho = -1/r$ and introduce the differential operators

$$\mathcal{L}_s = \partial_\theta + \frac{m}{\sin\theta} + s \cot\theta, \quad (\text{A7})$$

$$J_\pm = \partial_r \pm i \frac{\omega}{f}. \quad (\text{A8})$$

The quantities $T_{nn} \equiv T_{\mu\nu} n^\mu n^\nu$, $T_{n\bar{m}} \equiv T_{\mu\nu} n^\mu \bar{m}^\nu$, and $T_{\bar{m}\bar{m}} \equiv T_{\mu\nu} \bar{m}^\mu \bar{m}^\nu$ are contractions of $T^{\mu\nu}$ with the Kinnersley tetrad “legs”

$$n_\mu = -\frac{1}{2} (f(r), 1, 0, 0), \quad (\text{A9})$$

$$\bar{m}_\mu = -\frac{1}{\sqrt{2}r} (0, 0, -r^2, ir^2 \sin\theta), \quad (\text{A10})$$

and an overbar denotes complex conjugation. The explicit expressions are

$$\begin{aligned} T_{nn} &= \frac{\mu}{4r^2} \frac{1}{|\dot{r}|} (f(r) \dot{t} + \dot{r})^2 \delta(t - T(R)) \delta^2(\Omega - \Omega(R)), \\ T_{n\bar{m}} &= \frac{\mu}{2r^2} \frac{1}{|\dot{r}|} \frac{ir\dot{\phi}}{\sqrt{2}} (f(r) \dot{t} + \dot{r}) \delta(t - T(R)) \delta^2(\Omega - \Omega(R)), \\ T_{\bar{m}\bar{m}} &= -\frac{\mu}{2} \frac{\dot{\phi}^2}{|\dot{r}|} \delta(t - T(R)) \delta^2(\Omega - \Omega(R)). \end{aligned}$$

It is convenient to move the delta functions out of the operators by performing an integration by parts. To do that, note that given two functions A and B

$$\begin{aligned} \int d\Omega A \mathcal{L}_s B &= - \int d\Omega B \left(\partial_\theta - \frac{m}{\sin\theta} - (s-1) \cot\theta \right) A, \\ &\equiv -B \mathcal{L}_{-(s-1)}^+ A, \end{aligned} \quad (\text{A11})$$

where we assumed that the integrals exist and we defined

$$\mathcal{L}_s^+ = \partial_\theta - \frac{m}{\sin\theta} + s \cot\theta. \quad (\text{A12})$$

From the general properties of spin-weighted spherical harmonics [90] we get

$$\mathcal{L}_1^+ \mathcal{L}_2^+ {}_{-2}Y_{lm} = \sqrt{\lambda(\lambda+2)} {}_0Y_{lm} \quad (\text{A13})$$

$$\mathcal{L}_2^+ {}_{-2}Y_{lm} = -\sqrt{(l+2)(l-1)} {}_{-1}Y_{lm}, \quad (\text{A14})$$

where $\lambda \equiv (l-1)(l+2)$. Introducing the operator $L_+ \equiv \frac{d}{dr_*} + i\omega$, where the tortoise coordinate r_* is defined by $\frac{dr_*}{dr} = \frac{r^2}{\Delta}$, we can write $T_T = T_1 + T_2 + T_3$, with

$$\begin{aligned}
T_1 &\equiv -2 \int d\Omega dt (\rho^3 \mathcal{L}_{-1} [\rho^{-4} \mathcal{L}_0 (\rho^{-3} T_{nn})]) e^{i\omega t - im\phi} {}_{-2}Y_{lm}(\theta) = -\frac{\mu r^2}{2} \frac{e^{-im\phi + i\omega t}}{|\dot{r}|} (f(r) \dot{t} + \dot{r})^2 \mathcal{L}_1^+ \mathcal{L}_2^+ {}_{-2}Y_{lm}(\theta), \\
&= -\frac{\mu}{2r^2} \Delta^2 (V')^2 \dot{r} \sqrt{\lambda(\lambda+2)} e^{i\omega T - im\phi(R)} {}_0\bar{Y}_{lm}(\theta_0), \tag{A15}
\end{aligned}$$

$$\begin{aligned}
T_2 &\equiv 4 \int d\Omega \frac{\Delta^2 \rho^3}{2\sqrt{2}} e^{i\omega t - im\phi} {}_{-2}Y_{lm}(\theta) [\mathcal{L}_{-1} (\rho^{-2} J_+ (\Delta^{-1} \rho^{-4} T_{n\bar{m}})) + J_+ (\rho^{-2} \mathcal{L}_{-1} (\Delta^{-1} \rho^{-4} T_{n\bar{m}}))] \\
&= -i\mu \sqrt{\lambda} \Delta L_+ \left(r^2 \dot{\phi} V' e^{i\omega T - im\phi} \right) {}_{-1}\bar{Y}_{lm}(\theta_0), \tag{A16}
\end{aligned}$$

$$T_3 \equiv - \int d\Omega e^{i\omega t - im\phi} {}_{-2}Y_{lm}(\theta) \Delta^2 \rho^3 J_+ (\rho^{-4} J_+ (\rho^{-1} T_{\bar{m}\bar{m}})) = \frac{\Delta}{r} L_+ \left(\frac{r^6}{\Delta} L_+ \left(\frac{\mu r}{2\dot{r}} \dot{\phi}^2 e^{i\omega T - im\phi} \right) \right) {}_{-2}\bar{Y}_{lm}(\theta_0). \tag{A17}$$

Here we introduced the advanced coordinate $V \equiv t + r_*$ and we denoted radial derivatives with a prime (so $V' = dV/dr$).

In the Sasaki-Nakamura (SN) formalism [87–89] one introduces a new wave function $X_{lm}(r)$ related to the radial Teukolsky function of Eq. (A2) via

$$R_{lm} = \Delta L_+ \left(\frac{r^2}{\Delta} L_+ (r X_{lm}) \right). \tag{A18}$$

The function X_{lm} satisfies the differential equation (50), where the source term S_{lm} is related to the Teukolsky source T_T by the relation

$$\Delta L_+ \left(\frac{r^2}{\Delta} \right) L_+ \left(\frac{r^5 S_{lm}}{\Delta} \right) = -T_T. \tag{A19}$$

It is convenient to define a quantity

$$W_{lm} = \frac{r^5}{\Delta} S_{lm} e^{i\omega r_*}, \tag{A20}$$

which satisfies

$$\frac{d^2 W_{lm}}{dr^2} = -\frac{r^2}{\Delta^2} T_T e^{i\omega r_*}. \tag{A21}$$

By using the equality

$$e^{i\omega r_*} L_+ (X_{lm}(r) e^{i\omega T}) = \partial_{r_*} (X_{lm}(r) e^{i\omega V}), \tag{A22}$$

we can write $W_{lm} = W_1 + W_2 + W_3$, where

$$\begin{aligned}
\frac{d^2 W_1}{dr^2} &= \sqrt{\lambda(\lambda+2)} \frac{\mu}{2} (V')^2 \dot{r} e^{i\omega V - im\phi} {}_0\bar{Y}_{lm}(\theta_0), \\
\frac{d^2 W_2}{dr^2} &= i\mu \sqrt{\lambda} \partial_r \left(V' r^2 \dot{\phi} e^{i\omega V - im\phi} \right) {}_{-1}\bar{Y}_{lm}(\theta_0), \tag{A23} \\
\frac{d^2 W_3}{dr^2} &= -\frac{\mu}{r} \partial_r \left(r^4 \partial_r \left(\frac{r}{2} \dot{r}^{-1} \dot{\phi}^2 e^{i\omega V - im\phi} \right) \right) {}_{-2}\bar{Y}_{lm}(\theta_0).
\end{aligned}$$

Given any function $F(r)$ we have $F(r) V' e^{i\omega V} = 1/(i\omega)[(F e^{i\omega V})' - F' e^{i\omega V}]$. If we use this identity to integrate by parts, rearrange terms and set $\dot{r} = -\gamma$, these equations reduce to Eqs. (A5)–(A8) in Ref. [51].

1. Calculation of the Wronskian

From a numerical perspective, the integration of Eq. (50) is performed via a standard Green's function solution. For improved accuracy, in the numerical integrations we use asymptotic expansions of the wave functions near the horizon and near infinity. Close to $r = r_+ = 2M$ we set $y = \frac{(r-r_+)}{r_+}$, make the ansatz

$$X_{lm}(r) = e^{-i\omega r_*} \left[1 + \sum_{k=1}^{\infty} a_k y^k \right], \tag{A24}$$

and substitute into the differential equation (50). Noting that $f = y - y^2 + \mathcal{O}(y^3)$ we determine the leading-order and next-to-leading-order coefficients to be

$$\begin{aligned}
a_1 &= \frac{\lambda - 1}{1 - 4iM\omega}, \tag{A25} \\
a_2 &= \frac{3 + (\lambda - 1 + 8iM\omega)a_1}{4(1 - 2iM\omega)}.
\end{aligned}$$

In the limit $r \rightarrow \infty$ we have

$$X_{lm} \sim B_{lm}^{\text{in}} e^{i\omega r_*} \left[1 + \sum_{k=1}^{\infty} \frac{c_k}{r^k} \right] + A_{lm}^{\text{in}} e^{-i\omega r_*} \left[1 + \sum_{k=1}^{\infty} \frac{d_k}{r^k} \right]. \tag{A26}$$

The lowest-order coefficients in the series are found to be

$$c_1 = \frac{i(\lambda+2)}{2\omega}, \quad c_2 = -\frac{\lambda(\lambda+2) + 12iM\omega}{8\omega^2}, \tag{A27}$$

$$d_1 = -c_1, \quad d_2 = \frac{12iM\omega - \lambda(\lambda+2)}{8\omega^2}. \tag{A28}$$

One can invert these relations to get

$$\begin{aligned}
A_{lm}^{\text{in}} &= -r \frac{[(2M-r)(2c_2+c_1r) + ir^2(c_2+r(c_1+r))\omega] X_{lm}(r) - r(r-2M)[c_2+r(c_1+r)]X'_{lm}(r)}{(2M-r)[c_1d_2+2d_2r+(d_1-c_1)r^2-c_2(d_1+2r)] + 2r[c_2+r(c_1+r)][d_2+r(d_1+r)]\omega} e^{i\omega r_*}, \quad (\text{A29}) \\
B_{lm}^{\text{in}} &= ir \frac{[i(2M-r)(2d_2+d_1r) + r^2(d_2+r(d_1+r))\omega] X_{lm}(r) - ir(r-2M)[d_2+r(d_1+r)]X'_{lm}(r)}{(2M-r)[-c_1d_2-2d_2r+(c_1-d_1)r^2+c_2(d_1+2r)] + 2ir[c_2+r(c_1+r)][d_2+r(d_1+r)]\omega} e^{-i\omega r_*},
\end{aligned}$$

where a prime stands for a derivative with respect to r and in our numerics all quantities are evaluated at large but finite r (typically at $r = r_\infty = r_\infty^{(0)}/\omega$, with $r_\infty^{(0)} = 4 \times 10^4$). The Wronskian appearing in the Green's function solution of the inhomogeneous equation can be evaluated from the relation $W = 2i\omega A_{lm}^{\text{in}}$.

Appendix B: Multipolar decomposition of ZFL spectra

Here we discuss the extraction of multipolar components from the ZFL calculation. For consistency with the conventions we used in NR simulations [4, 6] and in the point-particle infalls discussed in this paper, we assume that the polarization states have an angular dependence that can be decomposed in spin-weighted spherical harmonics: $h_+ - ih_\times \sim \sum h_{lm-2} Y_{lm}$. Then (using the completeness of spin-weighted spherical harmonics) we can extract the multipolar content of the energy spectrum by equating

$$\frac{d^2 E}{d\omega d\Omega} = \left(\sum_{lm} \sqrt{\frac{dE_{lm}}{d\omega}} {}_{-2}Y_{lm} \right)^2, \quad (\text{B1})$$

where $dE_{lm}/d\omega$ are (as yet undetermined) functions of ω . From the orthonormality of spin-weighted spherical harmonics we find

$$\sqrt{\frac{dE_{lm}}{d\omega}} = \int d\Omega \sqrt{\frac{d^2 E}{d\omega d\Omega}} {}_{-2}Y_{lm}. \quad (\text{B2})$$

We now determine analytically the multipolar content of the radiation in the simple case of ultrarelativistic head-on collisions.

1. Equal mass collisions

If we assume that the collision occurs along the z -axis, the radiation will only contain $m = 0$ modes. For equal-

mass, ultrarelativistic head-on collisions Eq. (39) implies

$$\begin{aligned}
\frac{dE_{l0}}{d\omega} &= \frac{4E^2 M^2 (2l+1)(l-2)!}{\pi (l+2)!}, \quad l \text{ even} \\
&= 0, \quad l \text{ odd}. \quad (\text{B3})
\end{aligned}$$

Odd multipoles do not contribute, as required by equatorial symmetry. Summing over even multipoles we get $dE/d\omega = E^2 M^2/\pi$, in agreement with Smarr's Eq. (2.20) when $v \rightarrow c$ [20]. This expression assumes that the collision occurs along the z -axis, but the multipolar components in a general (rotated) frame can be found following the procedure discussed in Ref. [60].

2. Extreme-mass ratio collisions

From Eq. (46), for $\mu \equiv M_1 \ll M_2 \equiv M$ we get

$$\frac{dE_{l0}}{d\omega} = \frac{4E^2 \mu^2 (2l+1)(l-2)!}{\pi (l+2)!}. \quad (\text{B4})$$

Summing over multipoles we get $dE/d\omega = 4/(3\pi)E^2 \mu^2$, in agreement with Smarr's Eq. (2.18) when $v \rightarrow c$ [20].

We recall once more that Eq. (B4) is valid in a frame where the collision occurs along the z -axis, so only $m = 0$ modes are present. The transformation to a general (rotated) frame is explained in Ref. [60]. In the coordinate system used to compute the radiation from point particles falling into a Schwarzschild BH (section IV), and focusing on the dominant ($l = 2$) components, we get:

$$\frac{dE_{20}}{d\omega} = \frac{5E^2 \mu^2}{24\pi} = 0.0663146E^2 \mu^2, \quad (\text{B5})$$

$$\frac{dE_{22}}{d\omega} = \frac{5E^2 \mu^2}{16\pi} = 0.0994718E^2 \mu^2. \quad (\text{B6})$$

This is in excellent agreement with the point-particle results listed in Table I.

[1] F. Pretorius, Phys. Rev. Lett. **95**, 121101 (2005), gr-qc/0507014.
[2] J. G. Baker, J. Centrella, D.-I. Choi, M. Koppitz, and J. van Meter, Phys. Rev. Lett. **96**, 111102 (2006), gr-

qc/0511103.

[3] M. Campanelli, C. O. Lousto, P. Marronetti, and Y. Zlochower, Phys. Rev. Lett. **96**, 111101 (2006), gr-qc/0511048.

- [4] U. Sperhake, V. Cardoso, F. Pretorius, E. Berti, and J. A. Gonzalez, *Phys. Rev. Lett.* **101**, 161101 (2008), 0806.1738.
- [5] M. Shibata, H. Okawa, and T. Yamamoto, *Phys. Rev.* **D78**, 101501 (2008), 0810.4735.
- [6] U. Sperhake et al., *Phys. Rev. Lett.* **103**, 131102 (2009), 0907.1252.
- [7] M. W. Choptuik and F. Pretorius (2009), 0908.1780.
- [8] H. Yoshino and M. Shibata, *Phys. Rev.* **D80**, 084025 (2009), 0907.2760.
- [9] K.-i. Nakao, H. Abe, H. Yoshino, and M. Shibata, *Phys. Rev.* **D80**, 084028 (2009), 0908.0799.
- [10] M. Shibata and H. Yoshino (2009), 0912.3606.
- [11] M. Zilhao et al. (2010), 1001.2302.
- [12] V. Cardoso, E. Berti, and M. Cavaglia, *Class. Quant. Grav.* **22**, L61 (2005), hep-ph/0505125.
- [13] C. Merrick (2007), unpublished Junior Paper, Princeton University.
- [14] F. Pretorius and D. Khurana, *Class. Quant. Grav.* **24**, S83 (2007), gr-qc/0702084.
- [15] R. Grossman and J. Levin, *Phys. Rev.* **D79**, 043017 (2009), 0811.3798.
- [16] J. Healy, J. Levin, and D. Shoemaker, *Phys. Rev. Lett.* **103**, 131101 (2009), 0907.0671.
- [17] R. Gold and B. Bruegmann (2009), 0911.3862.
- [18] S. Weinberg, *Phys. Rev.* **135**, B1049 (1964).
- [19] S. Weinberg, *Phys. Rev.* **140**, B516 (1965).
- [20] L. Smarr, *Phys. Rev.* **D15**, 2069 (1977).
- [21] R. J. Adler and B. Zeks, *Phys. Rev.* **D12**, 3007 (1975).
- [22] R. Ruffini, *Phys. Rev.* **D7**, 972 (1973).
- [23] V. Ferrari and R. Ruffini, *Phys. Lett.* **B98**, 381 (1981).
- [24] C. O. Lousto and R. H. Price, *Phys. Rev.* **D55**, 2124 (1997), gr-qc/9609012.
- [25] V. Cardoso and J. P. S. Lemos, *Phys. Lett.* **B538**, 1 (2002), gr-qc/0202019.
- [26] V. Cardoso and J. P. S. Lemos, *Gen. Rel. Grav.* **35**, 327 (2003), gr-qc/0207009.
- [27] V. Cardoso and J. P. S. Lemos, *Phys. Rev.* **D67**, 084005 (2003), gr-qc/0211094.
- [28] E. Berti, M. Cavaglia, and L. Gualtieri, *Phys. Rev.* **D69**, 124011 (2004), hep-th/0309203.
- [29] J. D. Jackson, *Classical Electrodynamics* (J. Wiley, New York, 1975).
- [30] E. Berti, V. Cardoso, and C. M. Will, *Phys. Rev.* **D73**, 064030 (2006), gr-qc/0512160.
- [31] E. Berti, V. Cardoso, and A. O. Starinets, *Class. Quant. Grav.* **26**, 163001 (2009), 0905.2975.
- [32] P. Kanti, *Int. J. Mod. Phys.* **A19**, 4899 (2004), hep-ph/0402168.
- [33] S. Dimopoulos and G. L. Landsberg, *Phys. Rev. Lett.* **87**, 161602 (2001), hep-ph/0106295.
- [34] J. A. Frost et al., *JHEP* **10**, 014 (2009), 0904.0979.
- [35] M. Cavaglia, R. Godang, L. Cremaldi, and D. Summers, *Comput. Phys. Commun.* **177**, 506 (2007), hep-ph/0609001.
- [36] D.-C. Dai et al. (2009), 0902.3577.
- [37] R. H. Price and V. D. Sandberg, *Phys. Rev.* **D8**, 1640 (1973).
- [38] C. W. Misner, K. Thorne, and J. A. Wheeler, *Gravitation* (W. H. Freeman & Co., San Francisco, 1973).
- [39] J. M. Bardeen, W. H. Press, and S. A. Teukolsky, *Astrophys. J.* **178**, 347 (1972).
- [40] R. C. Myers and M. J. Perry, *Ann. Phys.* **172**, 304 (1986).
- [41] V. Cardoso, A. S. Miranda, E. Berti, H. Witek, and V. T. Zanchin, *Phys. Rev.* **D79**, 064016 (2009), 0812.1806.
- [42] M. Abramowitz and I. A. Stegun, *Handbook of Mathematical Functions with Formulas, Graphs, and Mathematical Tables* (Dover, New York, 1972).
- [43] S. Weinberg, *Gravitation and Cosmology* (J. Wiley, New York, 1972).
- [44] E. Poisson, *Phys. Rev.* **D47**, 1497 (1993).
- [45] T. Nakamura, K. Oohara, and Y. Kojima, *Prog. Theor. Phys. Suppl.* **90**, 1 (1987).
- [46] E. Berti et al., *Phys. Rev.* **D76**, 064034 (2007), gr-qc/0703053.
- [47] M. Davis, R. Ruffini, W. H. Press, and R. H. Price, *Phys. Rev. Lett.* **27**, 1466 (1971).
- [48] M. Davis, R. Ruffini, J. Tiomno, and F. Zerilli, *Phys. Rev. Lett.* **28**, 1352 (1972).
- [49] S. L. Detweiler, *Astrophys. J.* **225**, 687 (1978).
- [50] L. Smarr, *Sources of Gravitational Radiation* (Cambridge University Press, Cambridge, England, 1979), ISBN 0-521-22778-X.
- [51] K. I. Oohara and T. Nakamura, *Prog. Theor. Phys.* **70**, 757 (1983).
- [52] K. i. Oohara and T. Nakamura, *Phys. Lett.* **A94**, 349 (1983).
- [53] K. I. Oohara and T. Nakamura, *Prog. Theor. Phys.* **71**, 91 (1984).
- [54] K. Oohara, *Prog. Theor. Phys.* **71**, 738 (1984).
- [55] Y. Kojima and T. Nakamura, *Phys. Lett.* **A96**, 335 (1983).
- [56] Y. Kojima and T. Nakamura, *Phys. Lett.* **A99**, 37 (1983).
- [57] Y. Kojima and T. Nakamura, *Prog. Theor. Phys.* **71**, 79 (1984).
- [58] Y. Kojima and T. Nakamura, *Prog. Theor. Phys.* **72**, 494 (1984).
- [59] W. H. Press, S. A. Teukolsky, W. T. Vetterling, and B. P. Flannery, *Numerical Recipes in C++ - The Art of Scientific Computing - Third Edition* (Cambridge University Press, 2007), ISBN 0-521-75033-4.
- [60] L. Gualtieri, E. Berti, V. Cardoso, and U. Sperhake (2008), 0805.1017.
- [61] E. Berti, V. Cardoso, L. Gualtieri, F. Pretorius, and U. Sperhake, *Phys. Rev. Lett.* **103**, 239001 (2009), 0911.2243.
- [62] W. H. Press, *Astrophys. J.* **L170**, 105 (1971).
- [63] B. Mashhoon, *Phys. Rev.* **D31**, 290 (1985).
- [64] E. Berti and K. D. Kokkotas, *Phys. Rev.* **D71**, 124008 (2005), gr-qc/0502065.
- [65] L. Gualtieri, E. Berti, J. A. Pons, G. Miniutti, and V. Ferrari, *Phys. Rev.* **D64**, 104007 (2001), gr-qc/0107046.
- [66] J. A. Pons, E. Berti, L. Gualtieri, G. Miniutti, and V. Ferrari, *Phys. Rev.* **D65**, 104021 (2002), gr-qc/0111104.
- [67] P. Pani, E. Berti, V. Cardoso, Y. Chen, and R. Norte (2010), 1001.3031.
- [68] N. Yunes and E. Berti, *Phys. Rev.* **D77**, 124006 (2008), 0803.1853.
- [69] C. Cutler, D. Kennefick, and E. Poisson, *Phys. Rev.* **D50**, 3816 (1994).
- [70] V. I. Arnold, V. V. Kozlov, A. I. Neishtadt, and E. Khukhro, *Mathematical Aspects of Classical and Celestial Mechanics* (Springer, 2006).
- [71] P. C. Peters, *Phys. Rev.* **D1**, 1559 (1970).
- [72] R. V. Wagoner and C. M. Will, *Astrophys. J.* **210**, 764 (1976).

- [73] M. Turner, *Astrophys. J.* **216**, 610 (1977).
- [74] M. Turner and C. M. Will, *Astrophys. J.* **220**, 1107 (1978).
- [75] G. E. Curtis, *General Relativity and Gravitation* **9**, 999 (1978).
- [76] P. D. D'Eath, *Phys. Rev.* **D18**, 990 (1978).
- [77] P. D. D'Eath and P. N. Payne, *Phys. Rev.* **D46**, 658 (1992).
- [78] P. D. D'Eath and P. N. Payne, *Phys. Rev.* **D46**, 675 (1992).
- [79] P. D. D'Eath and P. N. Payne, *Phys. Rev.* **D46**, 694 (1992).
- [80] E. B. Segalis and A. Ori, *Phys. Rev.* **D64**, 064018 (2001), gr-qc/0101117.
- [81] R. A. Matzner and Y. Nutku, *Proc. Roy. Soc. Lond.* **336**, 285 (1974).
- [82] K. S. Thorne and S. J. Kovacs, *Astrophys. J.* **200**, 245 (1975).
- [83] R. J. Crowley and K. S. Thorne, *Astrophys. J.* **215**, 624 (1977).
- [84] S. J. Kovacs and K. S. Thorne, *Astrophys. J.* **217**, 252 (1977).
- [85] S. J. Kovacs and K. S. Thorne, *Astrophys. J.* **224**, 62 (1978).
- [86] H. Yoshino, T. Shiromizu, and M. Shibata, *Phys. Rev.* **D74**, 124022 (2006), gr-qc/0610110.
- [87] M. Sasaki and T. Nakamura, *Phys. Lett.* **A87**, 85 (1981).
- [88] M. Sasaki and T. Nakamura, *Phys. Lett.* **A89**, 68 (1982).
- [89] M. Sasaki and T. Nakamura, *Prog. Theor. Phys.* **67**, 1788 (1982).
- [90] J. N. Goldberg, A. J. MacFarlane, E. T. Newman, F. Rohrlich, and E. C. G. Sudarshan, *J. Math. Phys.* **8**, 2155 (1967).